



The ALMA Spectroscopic Survey in the HUDF: Nature and Physical Properties of Gas-mass Selected Galaxies Using MUSE Spectroscopy

Leindert A. Boogaard¹ , Roberto Decarli² , Jorge González-López^{3,4} , Paul van der Werf¹ , Fabian Walter^{5,6} , Rychard Bouwens¹ , Manuel Aravena³ , Chris Carilli^{6,7} , Franz Erik Bauer^{4,8,9} , Jarle Brinchmann^{1,10} , Thierry Contini¹¹ , Pierre Cox¹², Elisabete da Cunha¹³ , Emanuele Daddi¹⁴ , Tanio Díaz-Santos³ , Jacqueline Hodge¹ , Hanae Inami^{15,16}, Rob Ivison^{17,18} , Michael Maseda¹ , Jorryt Matthee¹⁹ , Pascal Oesch²⁰ , Gergő Popping⁵ , Dominik Riechers^{5,21} , Joop Schaye¹ , Sander Schouws¹, Ian Smail²² , Axel Weiss²³ , Lutz Wisotzki²⁴, Roland Bacon¹⁵, Paulo C. Cortes^{25,26} , Hans-Walter Rix⁵ , Rachel S. Somerville^{27,28}, Mark Swinbank²², and Jeff Wagg²⁹

¹Leiden Observatory, Leiden University, P.O. Box 9513, NL-2300 RA Leiden, The Netherlands; boogaard@strw.leidenuniv.nl

²INAF-Osservatorio di Astrofisica e Scienza dello Spazio, via Gobetti 93/3, I-40129, Bologna, Italy

³Núcleo de Astronomía de la Facultad de Ingeniería y Ciencias, Universidad Diego Portales, Av. Ejército Libertador 441, Santiago, Chile

⁴Instituto de Astrofísica, Facultad de Física, Pontificia Universidad Católica de Chile Av. Vicuña Mackenna 4860, 782-0436 Macul, Santiago, Chile

⁵Max Planck Institute für Astronomie, Königstuhl 17, D-69117 Heidelberg, Germany

⁶National Radio Astronomy Observatory, Pete V. Domenici Array Science Center, P.O. Box O, Socorro, NM 87801, USA

⁷Battcock Centre for Experimental Astrophysics, Cavendish Laboratory, Cambridge CB3 0HE, UK

⁸Millennium Institute of Astrophysics (MAS), Nuncio Monseñor Sótero Sanz 100, Providencia, Santiago, Chile

⁹Space Science Institute, 4750 Walnut Street, Suite 205, Boulder, CO 80301, USA

¹⁰Instituto de Astrofísica e Ciências do Espaço, Universidade do Porto, CAUP, Rua das Estrelas, PT4150-762 Porto, Portugal

¹¹Institut de Recherche en Astrophysique et Planétologie (IRAP), Université de Toulouse, CNRS, UPS, F-31400 Toulouse, France

¹²Institut d'astrophysique de Paris, Sorbonne Université, CNRS, UMR 7095, 98 bis bd Arago, F-7014 Paris, France

¹³Research School of Astronomy and Astrophysics, Australian National University, Canberra, ACT 2611, Australia

¹⁴Laboratoire AIM, CEA/DSM-CNRS-Université Paris Diderot, Irfu/Service d'Astrophysique, CEA Saclay, Orme des Merisiers, F-91191 Gif-sur-Yvette cedex, France

¹⁵Univ. Lyon 1, ENS de Lyon, CNRS, Centre de Recherche Astrophysique de Lyon (CRAL) UMR5574, F-69230 Saint-Genis-Laval, France

¹⁶Hiroshima Astrophysical Science Center, Hiroshima University, 1-3-1 Kagamiyama, Higashi-Hiroshima, Hiroshima, 739-8526, Japan

¹⁷European Southern Observatory, Karl-Schwarzschild-Strasse 2, D-85748, Garching, Germany

¹⁸Institute for Astronomy, University of Edinburgh, Royal Observatory, Blackford Hill, Edinburgh EH9 3HJ, UK

¹⁹Department of Physics, ETH Zurich, Wolfgang-Pauli-Strasse 27, 8093, Zurich, Switzerland

²⁰Department of Astronomy, University of Geneva, Ch. des Maillettes 51, 1290 Versoix, Switzerland

²¹Cornell University, 220 Space Sciences Building, Ithaca, NY 14853, USA

²²Centre for Extragalactic Astronomy, Department of Physics, Durham University, South Road, Durham, DH1 3LE, UK

²³Max-Planck-Institut für Radioastronomie, Auf dem Hügel 69, D-53121 Bonn, Germany

²⁴Leibniz-Institut für Astrophysik Potsdam, An der Sternwarte 16, D-14482 Potsdam, Germany

²⁵Joint ALMA Observatory—ESO, Av. Alonso de Córdova, 3104, Santiago, Chile

²⁶National Radio Astronomy Observatory, 520 Edgemont Road, Charlottesville, VA 22903, USA

²⁷Department of Physics and Astronomy, Rutgers, The State University of New Jersey, 136 Frelinghuysen Road, Piscataway, NJ 08854, USA

²⁸Center for Computational Astrophysics, Flatiron Institute, 162 5th Avenue, New York, NY 10010, USA

²⁹SKA Organization, Lower Withington Macclesfield, Cheshire SK11 9DL, UK

Received 2018 December 21; revised 2019 March 18; accepted 2019 April 12; published 2019 September 11

Abstract

We discuss the nature and physical properties of gas-mass selected galaxies in the ALMA spectroscopic survey (ASPECS) of the Hubble Ultra Deep Field (HUDF). We capitalize on the deep optical integral-field spectroscopy from the Multi Unit Spectroscopic Explorer (MUSE) HUDF Survey and multiwavelength data to uniquely associate all 16 line emitters, detected in the ALMA data without preselection, with rotational transitions of carbon monoxide (CO). We identify 10 as CO(2–1) at $1 < z < 2$, 5 as CO(3–2) at $2 < z < 3$, and 1 as CO(4–3) at $z = 3.6$. Using the MUSE data as a prior, we identify two additional CO(2–1) emitters, increasing the total sample size to 18. We infer metallicities consistent with (super-)solar for the CO-detected galaxies at $z \leq 1.5$, motivating our choice of a Galactic conversion factor between CO luminosity and molecular gas mass for these galaxies. Using deep *Chandra* imaging of the HUDF, we determine an X-ray AGN fraction of 20% and 60% among the CO emitters at $z \sim 1.4$ and $z \sim 2.6$, respectively. Being a CO-flux-limited survey, ASPECS-LP detects molecular gas in galaxies on, above, and below the main sequence (MS) at $z \sim 1.4$. For stellar masses $\geq 10^{10}$ ($10^{10.5}$) M_{\odot} , we detect about 40% (50%) of all galaxies in the HUDF at $1 < z < 2$ ($2 < z < 3$). The combination of ALMA and MUSE integral-field spectroscopy thus enables an unprecedented view of MS galaxies during the peak of galaxy formation.

Key words: galaxies: high-redshift – galaxies: ISM – galaxies: star formation

1. Introduction

Star formation takes place in the cold interstellar medium (ISM) and studying the cold molecular gas content of galaxies is therefore fundamental for our understanding of the formation and evolution of galaxies. As there is little to no emission from the molecular hydrogen that constitutes the majority of the

molecular gas in mass, cold molecular gas is typically traced by molecules, such as the bright rotational transitions of $^{12}\text{C}^{16}\text{O}$ (hereafter CO).

Recent years have seen a tremendous advance in the characterization of the molecular gas content of high-redshift galaxies (for a review, see Carilli & Walter 2013). Targeted

surveys with the Atacama Large Millimetre Array (ALMA) and the Plateau de Bure Interferometer (PdBI) have been instrumental in our understanding of the increasing molecular gas reservoirs of star-forming galaxies at $z > 1$ (Daddi et al. 2010, 2015; Genzel et al. 2010; Tacconi et al. 2010, 2013; Silverman et al. 2015, 2018). Combining data across cosmic time, these provide constraints on how the molecular gas content of galaxies evolves as a function of their physical properties, such as stellar mass (M_*) and star formation rate (SFR; Tacconi et al. 2013, 2018; Scoville et al. 2014, 2017; Genzel et al. 2015; Saintonge et al. 2016). These surveys typically target galaxies with SFRs that are greater than or equal to the majority of the galaxy population at their respective redshifts and stellar masses (the “main sequence” of star-forming galaxies; Brinchmann et al. 2004; Noeske et al. 2007; Whitaker et al. 2014; Schreiber et al. 2015; Boogaard et al. 2018; Eales et al. 2018), and therefore should be complemented by studies that do not rely on such a preselection.

Spectral line scans in the (sub)millimeter regime in deep fields provide a unique window into the molecular gas content of the universe. As the cosmic volume probed is well defined, these scans play a fundamental role in determining the evolution of the cosmic molecular gas density through cosmic time. Through their spectral scan strategy, these surveys are designed to detect molecular gas in galaxies without any preselection, providing a flux-limited view of the molecular gas emission at different redshifts (Decarli et al. 2014, 2016; Walter et al. 2014, 2016; Pavesi et al. 2018; Riechers et al. 2019). By conducting “spectroscopy-of-everything,” these can in principle reveal the molecular gas content in galaxies that would not be selected in traditional studies (e.g., galaxies with a low SFR, well below the main sequence (MS), but with a substantial gas mass).

This paper is part of a series of papers presenting the first results from the ALMA Spectroscopic Survey Large Program (ASPECS-LP; Decarli et al. 2019). The ASPECS-LP is a spectral line scan targeting the *Hubble* Ultra Deep Field (HUDF). Here we use the results from the spectral scan of Band 3 (84–115 GHz; 3.6–2.6 mm) and investigate the nature and physical properties of galaxies detected in molecular emission lines by ALMA. In order to do so, it is important to know about the physical conditions of the galaxies detected in molecular gas, such as their ISM conditions, their (*HST*) morphology, and their stellar and ionized gas dynamics. The HUDF benefits from the deepest and most extensive multiwavelength data, and, recently, ultra-deep integral-field spectroscopy.

A critical step in identifying ALMA emission lines with actual galaxies relies on matching the galaxies in redshift. In this context, the Multi Unit Spectroscopic Explorer (MUSE; Bacon et al. 2010) HUDF survey, which provides a deep optical integral-field spectroscopic survey over the HUDF (Bacon et al. 2017), is essential. The MUSE HUDF is a natural complement to the ASPECS-LP in the same area on the sky, providing optical spectroscopy for all galaxies within the field of view, also without any preselection. In addition, the integral-field spectrograph provides redshifts for over a thousand galaxies in the HUDF (increasing the number of previously known redshifts by a factor of $\sim 10\times$; Inami et al. 2017). Depending on the redshift, these data can provide key information on the ISM conditions (such as metallicity and

dynamics) of the galaxies harboring molecular gas. As we will see throughout this paper, the MUSE data are a significant step forward in our understanding of galaxy population selected with ALMA.

The paper is organized as follows: we first introduce the spectroscopic and multiwavelength data (Section 2). We discuss the redshift identification of the CO-detected galaxies from the line search (Gonzalez-Lopez et al. 2019), using the MUSE and multiwavelength data, in Section 3.1. Next, we leverage the large number of MUSE redshifts to separate real from spurious sources down to a significantly lower signal-to-noise ratio (S/N) than possible in the line search (Section 3.2). Together, these sources form the full ASPECS-LP Band 3 sample (Section 3.3). We then move on to the central question(s) of this paper: by doing a survey of molecular gas, in what kinds of galaxies do we detect molecular gas emission at different redshifts, and what are the physical properties of these galaxies? We determine stellar masses, SFRs, and (where possible) metallicities for all sources in Section 4 and link these to the molecular gas content (M_{mol}) to derive the gas fraction (M_{mol}/M_* , the molecular-to-stellar mass ratio) and depletion time ($t_{\text{depl}} = M_{\text{mol}}/\text{SFR}$). We first discuss the properties of the sample of CO-detected galaxies in the context of the overall population of the HUDF (Section 5.1) and investigate the X-ray AGN fraction among the detected sources (Section 5.2). Using the MUSE spectra, we determine the unobscured SFR (Section 5.3) and the metallicity of the $1 < z < 1.5$ sources (Section 5.4). Finally, we discuss the CO-detected galaxies from the flux-limited survey in the context of the galaxy MS (Section 6), focusing on the molecular gas mass, gas fraction, and depletion time. We discuss what fraction of the galaxy population in the HUDF we detect with increasing redshift. A further discussion of the molecular gas properties of these sources will be presented in Aravena et al. (2019).

Throughout this paper, we adopt a Chabrier (2003) IMF and a flat Λ CDM cosmology, with $H_0 = 70 \text{ km s}^{-1} \text{ Mpc}^{-1}$, $\Omega_m = 0.3$, and $\Omega_\Lambda = 0.7$. Magnitudes are in the AB system (Oke & Gunn 1983).

2. Observations

2.1. ALMA Spectroscopic Survey

We focus on the ASPECS-LP Band 3 observations that have been completed in ALMA Cycle 4. The acquisition and reduction of the Band 3 data are described in detail in Decarli et al. (2019). The final mosaic covers a 4.6 arcmin^2 area in the HUDF (where the primary beam response is $>50\%$ of the peak sensitivity). The data are combined into a single spectral cube with a spatial resolution of $\approx 1''.75 \times 1''.49$ (synthesized beam with natural weighting at 99.5 GHz) and a spectral resolution of 7.813 MHz, corresponding to $\Delta v \approx 23.5 \text{ km s}^{-1}$ at 99.5 GHz. The average root-mean-square (rms) sensitivity is $\approx 0.2 \text{ mJy beam}^{-1}$ but varies across the frequency range, being deepest ($\approx 0.13 \text{ mJy beam}^{-1}$) around 100 GHz and higher above 110 GHz, due to the spectral setup of the observations (see Gonzalez-Lopez et al. 2019 for details). Throughout this paper, we consider the area that lies within $>40\%$ of the primary beam peak sensitivity, which is the shallowest part of the survey over which we still detect CO candidates without preselection (Section 3.1). When comparing to the *HST* reference frame, we take into account an astrometric offset of $\Delta\alpha = +0''.076$, $\Delta\delta = -0''.279$ (Rujopakarn et al. 2016; Dunlop et al. 2017).

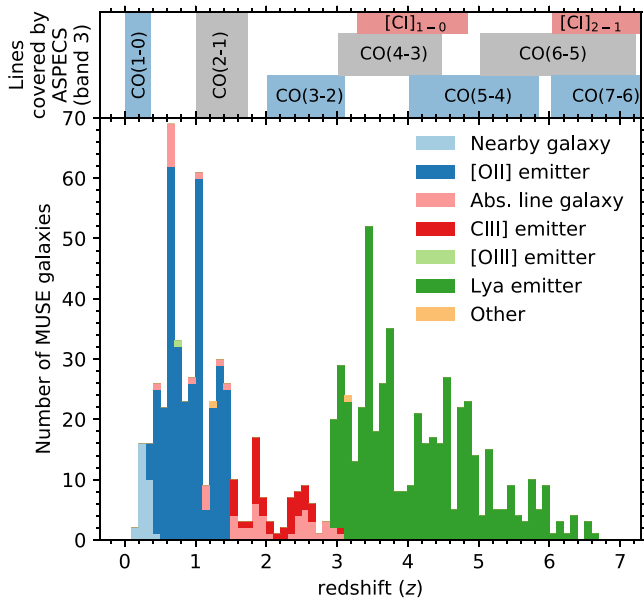


Figure 1. Molecular line redshift coverage of the galaxies in the MUSE and ASPECS-LP Hubble Ultra Deep Field (HUDF). The histogram shows the galaxies with spectroscopic redshifts from MUSE (*udf10* and *mosaic*; see Section 2.2) that lie within $>40\%$ of the primary beam sensitivity of the ASPECS-LP mosaic, distinguished by the primary spectral feature used to identify the redshift (Inami et al. 2017; “Nearby galaxy” summarizes a range of rest-frame optical features). The decrease in the number of redshifts between $1.5 < z < 2.9$ is due to the lack of strong emission line features in the MUSE spectrograph (“redshift desert”). The drop at the lowest redshifts is due to the nature and volume of the HUDF. The top panel shows the specific CO and [C I] transitions covered by the frequency setup of ASPECS Band 3 at different redshifts (Walter et al. 2016; Decarli et al. 2019). ASPECS covers CO(2–1) for [O II] emitters and absorption line galaxies at $1.0 < z < 1.74$. Galaxies with CO(3–2) at $2.0 < z < 3.11$ are identified mostly by UV absorption and weaker emission lines (e.g., C III). For higher-order CO and [C I] transitions above $z > 2.90$, MUSE has coverage of Ly α .

We perform an extensive search of the cube for molecular emission lines, as is detailed in Gonzalez-Lopez et al. (2019) and Section 3. With the Band 3 data alone, the ASPECS-LP is sensitive to different CO and [C I] transitions at specific redshift ranges, which are indicated in the top panel of Figure 1.

2.2. MUSE HUDF Survey

The HUDF was observed with the MUSE as part of the MUSE *Hubble* Ultra Deep Field survey (Bacon et al. 2017). The location on the sky of the ASPECS-LP with respect to the MUSE HUDF is shown in Decarli et al. (2019), Figure 1. The MUSE integral-field spectrograph has a $1' \times 1'$ field of view, covering the optical regime (4750–9300 Å) at an average spectral resolution of $\lambda/\Delta\lambda \approx 3000$. The HUDF was observed in a two-tier strategy, with the *mosaic*-region reaching a median depth of 10 hr in a $3' \times 3'$ region and the *udf10*-pointing reaching 31 hr depth in a $1' \times 1'$ region (3σ emission line depth for a point source of 3.1 and 1.5×10^{-19} erg s $^{-1}$ cm $^{-2}$ at 7000 Å, respectively). The data acquisition and reduction as well as the automated source detection are described in detail in Bacon et al. (2017). The measured seeing in the reduced data cube is $0''.65$ full width at half maximum (FWHM) at 7000 Å.

Redshifts were identified semiautomatically and the full spectroscopic catalog is presented in Inami et al. (2017). The spectra were extracted using a weighted extraction, where the weighting was based on the MUSE white light image, to obtain the maximal signal-to-noise. The spectra are modeled with a

modified version of PLATEFIT (Brinchmann et al. 2004, 2008; Tremonti et al. 2004) to obtain line-flux measurements and equivalent widths for all sources. The typical uncertainty on the redshift measurement is $\sigma_v = 0.00012(1+z)$ or ≈ 40 km s $^{-1}$ (Inami et al. 2017), which we use to compute the uncertainties in the relative velocities.

In order to compare in detail the relative velocities measured between the UV/optical features in MUSE and CO in ALMA, we need to place both on the same reference frame. The MUSE redshifts are provided in the barycentric reference frame, while the ALMA cube is set to the kinematic local standard of rest (LSRK). When determining detailed velocity offsets we place both on the same reference frame by removing the velocity difference; $\text{BARY-LSRK} = -16.7$ km s $^{-1}$ (accounting for the angle between the LSRK vector and the observation direction toward the HUDF).

The redshift distribution of the MUSE galaxies that fall within $>40\%$ of the primary beam peak sensitivity of the ASPECS-LP footprint in the HUDF is shown in Figure 1, where galaxies are color coded by the primary spectral feature(s) used to identify the redshift (see Inami et al. 2017 for details). The redshifts that correspond to the ASPECS band 3 coverage of the different molecular lines are indicated in the top panel. CO(1–0) [115.27 GHz] is observable at the lowest redshifts ($z < 0.3694$), where MUSE still covers a major part of the rest-frame optical spectrum that contains a wealth of spectral features, including absorption and (strong) emission lines (e.g., H α $\lambda 6563$, [O III] $\lambda 4959$, 5007, and [O II] $\lambda 3726$, 3729). The strong lines are the main spectral features used to identify star-forming galaxies all the way up to $z < 1.50$, where [O II] $\lambda 3726$, 3729 moves out of the spectral range of MUSE. CO(2–1) [230.54 GHz] is covered by ASPECS at $1.0059 < z < 1.7387$, mostly overlapping with [O II] in MUSE. At $z > 1.5$, the main features used to identify these galaxies are absorption lines such as Mg II $\lambda 2796$, 2803 and Fe II $\lambda 2586$, 2600. Over the redshift range of CO(3–2) [345.80 GHz], $2.0088 < z < 3.1080$, MUSE only has coverage of weaker UV emission lines (mainly C III] $\lambda 1907$, 1909), making redshift identifications more challenging (the “redshift desert”). Here, UV absorption lines are commonly used to identify redshifts, for galaxies where the continuum is strong enough ($m_{F775W} \lesssim 26$ mag). Above $z = 2.9$, MUSE flourishes again, with the coverage of Ly α $\lambda 1216$ all the way out to $z \approx 6.7$. Here, ASPECS covers CO(4–3) [461.04 GHz] and transitions with $J_{\text{up}} \geq 4$, and atomic carbon lines ([C I] $_{1-0}$ 610 μm and [C I] $_{2-1}$ 370 μm).

2.3. Multiwavelength Data (UV–Radio) and MAGPHYS

In order to construct spectral energy distributions (SEDs) for the ASPECS-LP sources, we utilize the wealth of available photometric data over the HUDF, summarized below.

We use the photometric compilation by Skelton et al. (2014, see references therein), which includes UV, optical, and near-IR photometry from the *Hubble Space Telescope* (HST) and ground-based facilities, as well as (deblended) *Spitzer*/IRAC 3.6, 4.5, 5.8, and 8.0 μm . We also include the corresponding deblended *Spitzer*/MIPS 24 μm photometry from Whitaker et al. (2014). We take deblended far-infrared (FIR) data from *Herschel*/PACS 100 and 160 μm from Elbaz et al. (2011), which have a native resolution of $6''.7$ and $11''.0$, respectively. The PACS 100 and 160 μm have a 3σ depth of 0.8 and 2.4 mJy and are limited by confusion. For the flux uncertainties we use the maximum of the local and simulated noise levels for each

source, as recommended by the documentation.³⁰ We further include the 1.2 mm continuum data from the combination of the available ASPECS-LP data with the ALMA observations by Dunlop et al. (2017), taken over the same region, as detailed in Aravena et al. (2019). We also include the ASPECS-LP 3.0 mm continuum data, as presented in Gonzalez-Lopez et al. (2019). For the ASPECS survey we have created a master photometry catalog for the galaxies in the HUDF, adopting the spectroscopic redshifts from MUSE (Section 2.2) and literature sources, as detailed in Decarli et al. (2019).

We use the high- z extension of the SED-fitting code MAGPHYS to infer physical parameters from the photometric information of the galaxies in our field (Da Cunha et al. 2008, 2015). The high- z extension of MAGPHYS includes a larger library of spectral emission models that extend to higher dust optical depths, higher SFRs and younger ages compared to what is typically found in the local universe. From the spectral emission models, the code can constrain the stellar mass, sSFR, and dust attenuation (A_V) along the line of sight. An energy-balance argument ensures that the amount of absorption at rest-frame UV/optical wavelengths is consistent with the light reradiated in the infrared. The code performs a Bayesian inference of the posterior likelihood distribution of the fitted parameter, to account for uncertainties such as degeneracies in the models, missing data, and nondetections.

We run MAGPHYS on all the galaxies in our catalog, using the available photometric information in all the bands (listed in Appendix B). We do not include the *Spitzer*/MIPS and *Herschel*/PACS photometry in the fits of the general sample because the angular resolution of these observations is relatively modest ($>5''$), thus a delicate deblending analysis would be required (the average sky density of galaxies in the HUDF is $\gtrsim 1$ galaxy per 3 arcsec^2). For the CO-detected galaxies we repeat the MAGPHYS fits including these bands (Section 4.1). In order to take into account systematic errors in the zero-point fitting for these sources, we add the zero-point errors (Skelton et al. 2014) in quadrature to the flux errors in all filters except *HST*, and include a 5% error-floor to further account for systematic errors in the physical models (following Leja et al. 2018). The filter selection of the general sample provides excellent photometric coverage of the stellar population. Paired with the wealth of spectroscopic redshifts (see Decarli et al. 2019 for a detailed description), this enables robust constraints on properties such as M_* , SFR, and A_V . We do note that while the formal uncertainties on the inferred properties are generally small, systematic uncertainties can be of order ~ 0.3 dex (e.g., Conroy 2013).

2.4. X-Ray Photometry

To identify AGN in the field, we use the *Chandra* X-ray data available over the GOODS-S region from Luo et al. (2017), which reaches the full depth of 7 Ms over the HUDF area. In total, there are 36 X-ray sources within the ASPECS-LP region of the HUDF (i.e., within 40% of the primary beam). We spatially cross-match the X-ray catalog to the closest source within $1''$ in our MUSE and multiwavelength catalog over the ASPECS-LP area, visually inspecting all matches used in this paper to ensure they are accurately identified.

At the depth of the X-ray data, there are multiple physical mechanisms (e.g., AGN and star formation) that may produce the X-ray emission detected at 0.5–7 keV. Luo et al. (2017) adopt the following six criteria to distinguish X-ray AGN from other sources of X-ray emission, of which at least one needs to be satisfied to be classified as AGN (we refer the reader to Xue et al. 2011; Luo et al. 2017 and references therein for details): (1) $L_X \geq 3 \times 10^{42} \text{ erg s}^{-1}$, identifying luminous X-ray sources; (2) an effective photon index $\Gamma_{\text{eff}} \leq 1.0$ indicating hard X-ray sources, identifying obscured AGN; (3) X-ray-to-R-band flux ratio of $\log(f_X/f_R) > -1$; (4) spectroscopically classified as AGN via, e.g., broad emission lines and/or high excitation lines; (5) X-ray-to-radio flux ratio of $L_X/L_{1.4 \text{ GHz}} \geq 2.4 \times 10^{18}$, indicating an excess of X-ray emission over the level expected from pure star formation; and (6) X-ray-to-K-band flux ratio of $\log(f_X/f_K) > -1.2$. Note that even with these criteria it is possible that some X-ray sources host low-luminosity or heavily obscured AGN and are currently misclassified.

Overall, there are six X-ray AGN in the ASPECS-LP volume at $1.0 < z < 1.7$, all of which have a MUSE redshift (one being a broad-line AGN). In the ASPECS-LP volume at $2.0 < z < 3.1$, there are seven X-ray AGN, three of which have spectroscopic redshifts from MUSE (including one broad-line AGN), and four with a photometric redshift (we discard one source in the catalog with a photometric redshift in this regime for which we cannot securely identify a counterpart in *HST*). There is one X-ray AGN at a higher redshift, which is also identified by MUSE as a broad-line AGN at $z = 3.188$.

3. The ASPECS-LP Sample

3.1. Identification of the Line Search Sample

An extensive description of the line search is provided in Gonzalez-Lopez et al. (2019). In summary, three independent methods were combined to search for CO lines in the ASPECS-LP band 3 data without any preselection: LINESEEKER (González-López et al. 2017), FINDCLUMP (Decarli et al. 2014; Walter et al. 2016), and MF3D (Pavesi et al. 2018). The fidelity³¹ of these line candidates was estimated from the ratio of the number of lines with a negative and positive flux detected at a given S/N. Lastly, the completeness of the sample was estimated by ingesting simulated emission lines into the real data cube.

In total, there are 16 emission line candidates for which the fidelity is ≥ 0.9 . Statistical analysis shows that this sample is free from false positives (the sum of their fidelities, based on the ALMA data alone, is 15.9; Gonzalez-Lopez et al. 2019). These 16 sources form the primary, *line search* sample and are shown in Figure 2. All these candidates have an S/N ≥ 6.4 .

For all sources in the primary sample, one or multiple potential counterpart galaxies are visible in the deep *HST* imaging shown in Figure 2. In order to confidently identify a single CO emission line, an independent redshift measurement of the potential counterpart measurement is needed. Given the wealth of multiwavelength photometry in the HUDF, photometric redshifts can often already provide sufficient constraints to discern between different rotation transitions of CO in the case of isolated galaxies at redshifts $z \lesssim 3$. However, complex systems of several galaxies, or projected superpositions of

³⁰ https://hedam.lam.fr/GOODS-Herschel/data/files/documentation/GOODS-Herschel_release.pdf

³¹ The fidelity is defined as $F = 1 - P$, where P is the probability of a line being produced by noise (Gonzalez-Lopez et al. 2019).

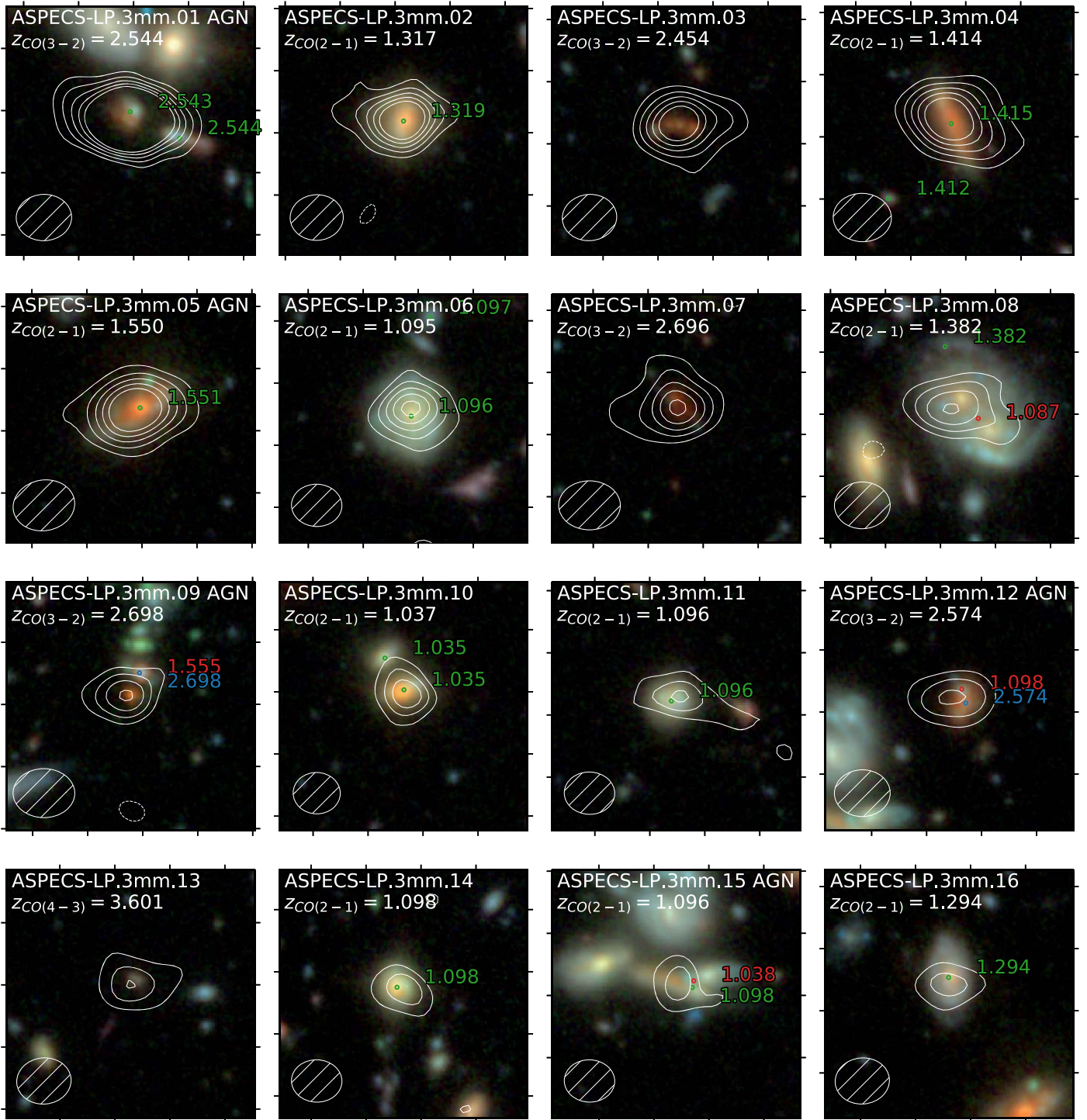


Figure 2. *HST* RGB cutouts (F160W, F125W, and F105W) of the 16 CO line detections from the line search, all revealing an optical/NIR counterpart. Each panel is $8'' \times 8''$ centered around the CO emission (corrected astrometry; Section 2.1). The white contours indicate the CO signal from $\pm[3, \dots, 11]\sigma$ in steps of 2σ . The ALMA beam is indicated in the bottom left corner. Galaxies with a spectroscopic redshift from MUSE (Inami et al. 2017) matching the CO signal are labeled in green (and red if not matching); spectroscopic redshifts in blue are newly determined in this paper. Of the 16 galaxies, 12 match closely to a redshift from MUSE (including ASPECS-LP.3mm.08, discussed in Appendix A and Decarli et al. 2016). ASPECS-LP.3mm.03, 3mm.07, and 3mm.09 have $m_{F775W} > 27$, which is too faint for a direct absorption line redshift from MUSE (but are independently confirmed). For ASPECS-LP.3mm.09 we do find UV absorption features matching the CO(3–2) in the galaxy slightly to the north. A new absorption line redshift is found for ASPECS-LP.3mm.12 (see Figure 18). The photometric redshift and absence of lower- z spectral features indicate ASPECS-LP.3mm.13 being at $z = 3.601$.

independent galaxies at distinct redshifts, can make redshift assignments more complicated. Fortunately, the integral-field spectroscopy from MUSE is ideally suited to disentangle spectral features belonging to different galaxies, allowing us to confidently assign redshifts to the CO emission lines. The

frequency of a CO line can correspond to different rotational transitions, each with a unique associated redshift. With the potential redshift solutions in hand, we systematically identify the CO line candidates from the line search. We provide a summary of the redshift identifications here. A detailed

description of the individual sources and their redshift identifications can be found in Appendix A, where we also show the MUSE spectra for all sources (Figures 13–16).

First, we correlate the spatial position and potential redshifts of the CO lines with known spectroscopic redshifts from MUSE (Inami et al. 2017). From the MUSE redshifts alone, we immediately identify most (11/16) of the CO lines with the highest fidelity. The brightest (ASPECS-LP.3mm.01) is a CO(3–2) emitter at $z = 2.54$, showing a wealth of UV absorption features. The other 10 galaxies are a diverse sample of CO(2–1) emitters spanning the redshift range over which we are sensitive: $1.01 < z < 1.74$. They show a variety of spectra at different levels of S/N, covering a range of UV and optical absorption and emission features. Notably, [O II] $\lambda 3726, 3729$ is detected in all galaxies where it is covered by MUSE, while [Ne III] $\lambda 3869$ is detected in some of the higher S/N spectra.

Next, we extract MUSE spectra for the remaining five (5/16) sources without a cataloged redshift and investigate their spectra for a redshift solution matching the observed CO line. We discover two new spectroscopic redshifts at $z = 2.54$ (ASPECS-LP.3mm.12) and $z = 2.69$ (associated with ASPECS-LP.3mm.09) confirming detections of CO(3–2), which were both not included in the catalog of Inami et al. (2017) as their spectra are blended with foreground sources. The former in particular demonstrates the key use of MUSE in disentangling a spatially overlapping system comprised of a foreground [O II] emitter and a faint background galaxy, which is detected at $S/N > 4$ both via cross-correlation with a $z \approx 2.5$ spectral template and by stacking absorption features (see Figure 18). For ASPECS-LP.3mm.03 and ASPECS-LP.3mm.07 we leverage the absence of spectral features (e.g., [O II], $\text{Ly}\alpha$), consistent with their faint magnitudes ($m_{F775W} > 27$ mag) and a redshift in the MUSE redshift desert, in combination with photometric redshifts in the $z = 2$ – 3 regime from the deep multiwavelength data, to confirm detections of CO(3–2). Lastly, we find ASPECS-LP.3mm.13 being CO(4–3) at $z = 3.601$, based on the photometric redshifts suggesting $z \approx 3.5$ and the absence of a lower redshift solution from the spectrum. $\text{Ly}\alpha \lambda 1216$ is not detected for this source, but we caution that at this redshift $\text{Ly}\alpha$ falls very close to the [O I] $\lambda 5577$ skyline. Furthermore, given that the source potentially contains significant amounts of dust, no $\text{Ly}\alpha$ emission may be expected at all.

In summary, we determine a redshift solution for all (16/16) candidates from the line search. Twelve are directly confirmed by MUSE spectroscopy, while the remaining four are supported by their photometric redshifts and indirect spectroscopic evidence. We highlight that some of these counterparts are very faint, even in the reddest *HST* bands, and their identifications would not have been possible without the exquisite depth of both the *HST* and MUSE data over the HUDF. Similar objects would typically not have robust photometric counterparts in areas of the sky with inferior coverage (let alone have independent spectroscopic confirmation).

The identifications of the CO transitions, along with their MUSE counterparts, are presented in Table 1. We show the spatial extent of the CO emission on top of the *HST* images in Figure 2. The MUSE spectra for the individual sources are shown in Figures 13–16 and discussed in Appendix A.

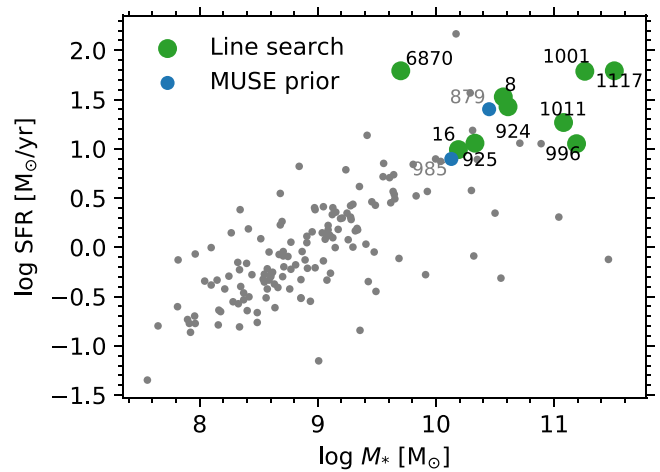


Figure 3. Stellar mass vs. SFR (from MAGPHYS) of all galaxies with a MUSE redshift at $1.01 < z < 1.74$ in the ASPECS-LP footprint. Leveraging the MUSE redshift as prior, we find a CO(2–1) signal in two additional galaxies (blue). The numbers indicate the MUSE IDs of the sources. The detections from the line search (green; Section 3.1) are also recovered in the prior-based search. By using the MUSE redshifts to search for CO at lower luminosities, we reveal molecular gas in most of the massive, star-forming galaxies at these redshifts.

3.2. Additional Sources with MUSE Redshift Priors at $z < 2.9$

The CO-line detections from Gonzalez-Lopez et al. (2019) are selected to have the highest fidelity and are therefore the highest S/N (≥ 6.4) candidates over the ASPECS-LP area. In Figure 3, we plot the stellar mass–SFR relation for all MUSE sources at $1.01 < z < 1.74$, where we indicate all the galaxies that have been detected in CO(2–1) in the line search.³² There are several galaxies in the field with properties similar to the ASPECS-LP galaxies that are not detected in the line search. This raises the following question: why are these galaxies not detected? Given their physical properties, we may expect some of these galaxies to harbor molecular gas and therefore to have CO signal in the ASPECS-LP cube. The reason that we did not detect these sources in the line search may, therefore, simply be due to the fact that they are present at lower S/N, which puts them in the regime where the decreasing fidelity makes it challenging to identify them among the spurious sources.

However, the physical properties of the galaxies themselves provide an extra piece of information that can guide us in detecting CO for these sources. In particular, we can use the spectroscopic redshifts from MUSE to obtain a measurement of the CO flux for each source, either identifying them at lower S/N, or putting an upper limit on their molecular gas mass. We aim at the CO transitions covered at $z < 2.9$, where the features in the MUSE spectrum typically provide a systemic redshift. At higher redshift the main spectral feature used to identify redshifts is often $\text{Ly}\alpha$, which can be offset from the systemic redshift by a few hundred km s^{-1} (e.g., Shapley et al. 2003; Rakic et al. 2011; Verhamme et al. 2018).

We extract a single-pixel spectrum from the $3''$ tapered cube at the position of each MUSE source in the redshift range, after correcting for the astrometric offset (Section 2.1). We then fit

³² Note that we do not show the MUSE source associated with ASPECS-LP.3mm.08 and the two MUSE sources that are severely blended with ASPECS-LP.3mm.12 and the galaxy north of ASPECS-LP.3mm.09 on the plot.

Table 1
ASPECS-LP CO-detected Sources from the Line Search, with MUSE Spectroscopic Counterparts

| ID | R.A. | Decl. | ν_{CO} | CO trans. | z_{CO} | MUSE ID | z_{MUSE} | Δv |
|--------|----------------|----------------|-------------------|---|---------------------|-------------------|---------------------|-------------------------------|
| (1) | (J2000) (2) | (J2000) (3) | (GHz) (4) | ($J_{\text{up}} \rightarrow J_{\text{low}}$) (5) | (6) | (7) | (8) | (km s^{-1}) (9) |
| 3mm.01 | 03:32:38.54 | -27:46:34.6 | 97.584 ± 0.003 | 3 → 2 | 2.5436 | 35 | 2.5432 | -15.5 ± 41.0 |
| 3mm.02 | 03:32:42.38 | -27:47:07.9 | 99.510 ± 0.005 | 2 → 1 | 1.3167 | 996 | 1.3172 ^a | 73.5 ± 42.7 |
| 3mm.03 | 03:32:41.02 | -27:46:31.5 | 100.131 ± 0.005 | 3 → 2 | 2.4534 | ... | ... | ... |
| 3mm.04 | 03:32:34.44 | -27:46:59.8 | 95.501 ± 0.006 | 2 → 1 | 1.4140 | 1117 | 1.4147 | 102.9 ± 44.2 |
| 3mm.05 | 03:32:39.76 | -27:46:11.5 | 90.393 ± 0.006 | 2 → 1 | 1.5504 | 1001 | 1.5509 | 71.7 ± 44.7 |
| 3mm.06 | 03:32:39.90 | -27:47:15.1 | 110.038 ± 0.005 | 2 → 1 | 1.0951 | 8 | 1.0955 | 79.2 ± 42.3 |
| 3mm.07 | 03:32:43.53 | -27:46:39.4 | 93.558 ± 0.008 | 3 → 2 | 2.6961 | ... | ... | ... |
| 3mm.08 | 03:32:35.58 | -27:46:26.1 | 96.778 ± 0.002 | 2 → 1 | 1.3821 | 6415 | 1.3820 | -0.1 ± 40.5 |
| 3mm.09 | 03:32:44.03 | -27:46:36.0 | 93.517 ± 0.003 | 3 → 2 | 2.6977 ^b | ... | ... | ... |
| 3mm.10 | 03:32:42.98 | -27:46:50.4 | 113.192 ± 0.009 | 2 → 1 | 1.0367 | 1011 | 1.0362 ^a | -53.7 ± 46.6 |
| 3mm.11 | 03:32:39.80 | -27:46:53.7 | 109.966 ± 0.003 | 2 → 1 | 1.0964 | 16 | 1.0965 | 19.8 ± 40.8 |
| 3mm.12 | 03:32:36.21 | -27:46:27.7 | 96.757 ± 0.004 | 3 → 2 | 2.5739 | 1124 ^c | 2.5739 ^a | 16.8 ± 41.9 |
| 3mm.13 | 03:32:35.56 | -27:47:04.3 | 100.209 ± 0.006 | 4 → 3 | 3.6008 | ... | ... | ... |
| 3mm.14 | 03:32:34.84 | -27:46:40.7 | 109.877 ± 0.009 | 2 → 1 | 1.0981 | 924 | 1.0981 | 15.0 ± 46.9 |
| 3mm.15 | 03:32:36.48 | -27:46:31.9 | 109.971 ± 0.005 | 2 → 1 | 1.0964 | 6870 | 1.0979 | 240.4 ± 42.3 |
| 3mm.16 | 03:32:39.92 | -27:46:07.4 | 100.503 ± 0.004 | 2 → 1 | 1.2938 | 925 | 1.2942 | 66.3 ± 41.7 |

Notes. The CO frequencies are taken from Gonzalez-Lopez et al. (2019). (1) ASPECS-LP 3mm ID. (2)–(3) Coordinates. (4) CO line frequency. (5) Identified CO transition (Section 3.1). (6) CO redshift. (7) MUSE ID. (8) MUSE redshift. (9) Velocity offset between MUSE and ALMA ($\Delta v = (z_{\text{MUSE}} - z_{\text{CO}})/(1 + z_{\text{CO}})$; after converting both to the same reference frame).

^a Updated from Inami et al. (2017), see Appendix A.

^b Additionally supported by matching absorption found in MUSE#6941, at $z = 2.695, 0''7$ to the north.

^c Additional redshift for MUSE#1124, which is cataloged as the foreground [O II]-emitter at $z = 1.098$ (see Figure 18).

the lines with a Gaussian curve, using a custom-made Bayesian Markov chain Monte Carlo routine with the following priors:

1. *line peak velocity*: a Gaussian distribution centered at $\Delta v = 0$ (based on the MUSE redshift) and $\sigma = 100 \text{ km s}^{-1}$ (the MUSE spectral resolution).
2. *line width*: a Maxwellian distribution with a width of 100 km s^{-1} .
3. *line flux*: a Gaussian distribution centered at zero, with $\sigma = 0.5 \text{ Jy km s}^{-1}$, allowing both positive and negative line fluxes to be fitted.

We choose a strong prior on the velocity difference, as we only search for lines at the exact MUSE redshift. The Gaussian prior on the line flux is important to estimate the fidelity of our measurements, allowing an unbiased comparison of positive versus negative line fluxes (see Gonzalez-Lopez et al. 2019 for details). The Maxwellian prior is chosen because it is bound to produce positive values of the line width, depends on a single scale parameter, and has a non-null tail at very large line widths. The uncertainties are computed from the 16th and 84th percentiles of the posterior distributions of each parameter.

As narrow lines are more easily caused by noise in the cube (Gonzalez-Lopez et al. 2019), we rerun the fit with a broader prior on the line width of 200 km s^{-1} . We also independently fit the spectrum with a uniform prior over $\pm 1 \text{ GHz}$ around the MUSE redshift. We select only the sources in which the same feature was recovered with $S/N > 3$ in all three fits. In order to select a sample that is as pure as possible, we select only the objects that have a velocity offset of $< 80 \text{ km s}^{-1}$ from the MUSE systemic redshift (≈ 2 the typical uncertainty on the MUSE redshift). In addition, we only keep objects with a line width of $> 100 \text{ km s}^{-1}$, to avoid including spurious narrow lines. We note that, while these cuts potentially remove other sources that are detected at lower S/N , we do not attempt to be

complete. Rather, we aim to have the prior-based sample as clean as possible.

The prior-based search reveals two additional sources detected in CO(2–1) with an $S/N > 3$ (see Table 2). Both sources lie within the area in which the sensitivity is $> 40\%$ of the primary beam peak sensitivity. We show the *HST* cutouts with the CO spectra of these sources in Figure 4, ordered by S/N . ASPECS-LP-MP.3mm.02 is the foreground spiral galaxy of ASPECS-LP.3mm.08. This source was already found in the ASPECS-Pilot (Decarli et al. 2016, see Appendix A).

Because the molecular gas mass is to first order correlated with the SFR, we expect to detect CO in the galaxies with the highest SFRs at a given redshift. Sorting all the galaxies by their SFR indeed reveals a clear correlation between the SFR and the S/N in CO, suggesting there are additional sources in the ASPECS-LP data cube at lower S/N . This can also be clearly seen from Figure 3, where our stringent sample of prior-based sources all lie at $\log \text{SFR}[M_{\odot} \text{ yr}^{-1}] > 0.5$. Qualitatively, it becomes clear that the ASPECS-LP is sensitive enough to detect molecular gas in most massive MS galaxies at $1.01 < z < 1.74$ (a quantitative discussion of the detection fraction for the full sample is provided in Section 6). For many galaxies, the reason these are not unveiled in the line search may simply be because their lower CO luminosity and/or smaller line width puts them below the conservative S/N threshold we adopt in the line search. Using the MUSE redshifts as prior information, it is possible to unveil their molecular gas reservoirs at lower S/N .

3.3. Full Sample Redshift Distribution

The full ASPECS-LP CO line sample consists of 18 galaxies with a CO detection in the HUDF; 16 detections without preselection and 2 MUSE redshift prior-based detections.

Table 2
ASPECS-LP CO(2–1) Detected Sources Based On a Spectroscopic Redshift Prior from MUSE

| ID | R.A. (J2000) | Decl. (J2000) | ν_{CO} (GHz) | CO trans. ($J_{\text{up}} \rightarrow J_{\text{low}}$) | z_{CO} | MUSE ID | z_{MUSE} | Δv (km s^{-1}) |
|-----------|-----------------|------------------|----------------------------|---|-----------------|---------|-------------------|--------------------------------------|
| (1) | (2) | (3) | (4) | (5) | (6) | (7) | (8) | (9) |
| MP.3mm.01 | 03:32:37.30 | -27:45:57.8 | 109.978 ± 0.011 | 2 \rightarrow 1 | 1.0962 | 985 | 1.0959 | -28.2 ± 50.6 |
| MP.3mm.02 | 03:32:35.48 | -27:46:26.5 | 110.456 ± 0.007 | 2 \rightarrow 1 | 1.0872 | 879 | 1.0874 | 55.8 ± 44.3 |

Note. (1) ASPECS-LP MUSE prior (MP) ID. (2)–(3) Coordinates. (4) CO line frequency. (5) CO transition. (6) CO redshift. (7) MUSE ID. (8) MUSE redshift. (9) Velocity offset between MUSE and ALMA ($\Delta v = (z_{\text{MUSE}} - z_{\text{CO}})/(1 + z_{\text{CO}})$; after converting both to the same reference frame).

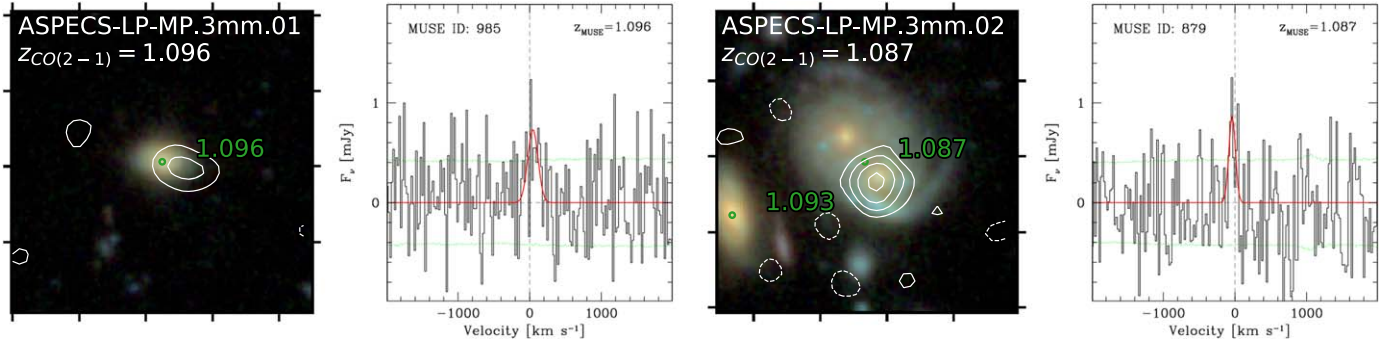


Figure 4. *HST* cutouts (F160W, F125W, and F105W) and CO(2–1) spectra for two additional CO line candidates, found through a MUSE redshift prior. The CO contours are shown in white starting at $\pm 2\sigma$ in steps of 1σ . All other labeling in the cutouts is the same as that in Figure 3. In the spectra the velocity is given relative to the MUSE redshift. The spectrum and best-fit Gaussian are shown in black and red, respectively. The local rms noise level is shown in green.

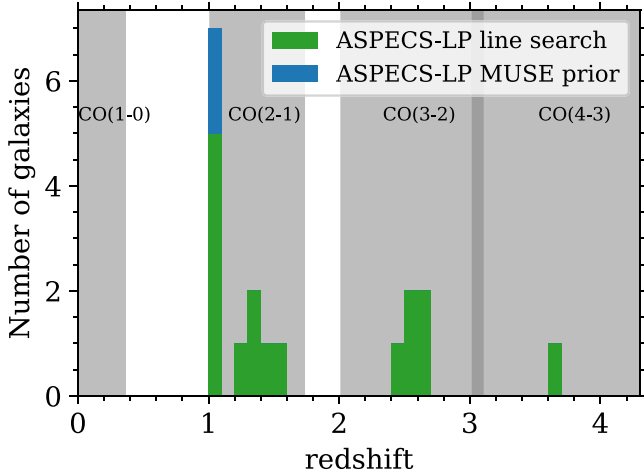


Figure 5. Redshift distribution of the ASPECS-LP CO-detected sources, which all have an *HST* counterpart. We show both the detections from the line search (Section 3) as well as the MUSE prior-based galaxies (Section 3.2). The gray shading indicates the redshift ranges over which we can detect different CO transitions.

These galaxies span a range of redshifts between $1 < z < 4$. The lowest redshift galaxy is detected in CO(2–1) at $z = 1.04$, while the highest redshift galaxy is detected (without prior) in CO(4–3) at $z = 3.60$. We show a histogram of the redshifts of the line-search and prior-based detections in Figure 5.

Twelve sources are detected in CO(2–1) at $1.01 < z < 1.74$, where the combination of molecular line sensitivity and survey volume are optimal. Most prominently, we detect five galaxies at the same redshift of $z \approx 1.1$. These galaxies are all part of an overdensity of galaxies in the HUDF at $z = 1.096$, visible in Figure 1.

Five sources are detected in CO(3–2) at $2.01 < z < 3.11$, including the brightest CO emitter in the field at $z = 2.54$ (ASPECS-LP.3mm.01; see also Decarli et al. 2016) and a pair of galaxies (ASPECS-LP.3mm.07 and #9) at $z \approx 2.697$ (see Section 3.1). All five CO(3–2) sources are detected in 1 mm dust continuum (Aravena et al. 2016; Dunlop et al. 2017) with flux densities below 1 mJy. However, only one of these sources (ASPECS-LP.3mm.01) previously had a spectroscopic redshift (Walter et al. 2016; Inami et al. 2017).

4. Physical Properties

4.1. SFRs from MAGPHYS and [O II]

For all the CO-detected sources, we derive the SFR (and M_* and A_V) from the UV-FIR data (including 24–160 μm and ASPECS-LP 1.2 and 3.0 mm) using MAGPHYS (see Section 2.3), which are provided in Table 3. The full SED fits are shown in Figure 19.

For the $1 < z < 1.5$ subsample, we have access to the [O II] $\lambda 3726, 3729$ -doublet. We derive SFRs from [O II] $\lambda 3726, 3729$ following Kewley et al. (2004), adopting a Chabrier (2003) IMF. The observed [O II] luminosity gives a measurement of the unobscured SFR, which can be compared to the total SFR (including the FIR) to derive the fraction of obscured star formation. For that reason, we do not apply a dust correction when calculating the SFR([O II]).

The derived SFR([O II] $\lambda 3726, 3729$) is dependent on the oxygen abundance. We have access to the oxygen abundance directly for some of the sources and can also make an estimate through the mass–metallicity relation (e.g., Zahid et al. 2014). However, because of the additional uncertainties in the calibrations for the oxygen abundance, we instead adopt an average [O II] $\lambda 3726, 3729/\text{H}\alpha$ ratio of unity, given that all our sources are massive and hence expected to have high oxygen abundance $12 + \log \text{O}/\text{H} \sim 8.8$, where $[\text{O II}]/\text{H}\alpha = 1.0$

Table 3
Physical Properties of the ASPECS-LP Sources from the Line Search and the MUSE Prior-based Search, with Formal Uncertainties

| ID | z | $\log M_{*,\text{SED}}$ (M_{\odot}) | SFR_{SED} ($M_{\odot} \text{ yr}^{-1}$) | $A_{V,\text{SED}}$ (mag) | X-ray | XID |
|---------------------|--------|--|--|-----------------------------|-------|-----|
| (1) | (2) | (3) | (4) | (5) | (6) | (7) |
| ASPECS-LP.3mm.01 | 2.5436 | $10.4^{+0.0}_{-0.0}$ | 233^{+0}_{-0} | $2.7^{+0.0}_{-0.0}$ | AGN | 718 |
| ASPECS-LP.3mm.02 | 1.3167 | $11.2^{+0.0}_{-0.0}$ | 11^{+5}_{-0} | $1.7^{+0.1}_{-0.0}$ | | |
| ASPECS-LP.3mm.03 | 2.4534 | $10.7^{+0.1}_{-0.1}$ | 68^{+19}_{-20} | $3.1^{+0.1}_{-0.3}$ | | |
| ASPECS-LP.3mm.04 | 1.4140 | $11.3^{+0.0}_{-0.0}$ | 61^{+3}_{-12} | $2.9^{+0.1}_{-0.0}$ | | |
| ASPECS-LP.3mm.05 | 1.5504 | $11.5^{+0.0}_{-0.0}$ | 62^{+5}_{-19} | $2.3^{+0.1}_{-0.3}$ | AGN | 748 |
| ASPECS-LP.3mm.06 | 1.0951 | $10.6^{+0.0}_{-0.0}$ | 34^{+0}_{-0} | $0.8^{+0.0}_{-0.0}$ | X | 749 |
| ASPECS-LP.3mm.07 | 2.6961 | $11.1^{+0.1}_{-0.1}$ | 187^{+35}_{-16} | $3.2^{+0.1}_{-0.1}$ | | |
| ASPECS-LP.3mm.08 | 1.3821 | $10.7^{+0.0}_{-0.0}$ | 35^{+8}_{-5} | $0.9^{+0.1}_{-0.1}$ | | |
| ASPECS-LP.3mm.09 | 2.6977 | $11.1^{+0.1}_{-0.0}$ | 318^{+35}_{-35} | $3.6^{+0.1}_{-0.1}$ | AGN | 805 |
| ASPECS-LP.3mm.10 | 1.0367 | $11.1^{+0.0}_{-0.1}$ | 18^{+1}_{-1} | $3.0^{+0.0}_{-0.1}$ | | |
| ASPECS-LP.3mm.11 | 1.0964 | $10.2^{+0.0}_{-0.0}$ | 10^{+0}_{-1} | $0.8^{+0.0}_{-0.1}$ | | |
| ASPECS-LP.3mm.12 | 2.5739 | $10.6^{+0.0}_{-0.1}$ | 31^{+18}_{-3} | $0.8^{+0.2}_{-0.1}$ | AGN | 680 |
| ASPECS-LP.3mm.13 | 3.6008 | $9.8^{+0.1}_{-0.1}$ | 41^{+15}_{-9} | $1.4^{+0.3}_{-0.2}$ | | |
| ASPECS-LP.3mm.14 | 1.0981 | $10.6^{+0.1}_{-0.1}$ | 27^{+1}_{-4} | $1.6^{+0.0}_{-0.2}$ | | |
| ASPECS-LP.3mm.15 | 1.0964 | $9.7^{+0.3}_{-0.0}$ | 62^{+0}_{-4} | $2.9^{+0.0}_{-0.0}$ | AGN | 689 |
| ASPECS-LP.3mm.16 | 1.2938 | $10.3^{+0.1}_{-0.0}$ | 11^{+3}_{-3} | $0.5^{+0.1}_{-0.2}$ | | |
| ASPECS-LP-MP.3mm.01 | 1.0959 | $10.1^{+0.1}_{-0.0}$ | 8^{+3}_{-2} | $1.3^{+0.2}_{-0.2}$ | | |
| ASPECS-LP-MP.3mm.02 | 1.0874 | $10.4^{+0.0}_{-0.0}$ | 25^{+0}_{-0} | $1.0^{+0.0}_{-0.0}$ | X | 661 |

Note. (1) ASPECS-LP ID number. (2) Source redshift. (3) Stellar mass (M_{*}). (4) Star formation rate (SFR). (5) Visual attenuation (A_V). (6)–(7) X-ray classification as active galactic nucleus (AGN) or other X-ray source (X) from Luo et al. (2017) and corresponding X-ray ID (XID).

Table 4
Emission Line Flux, Unobscured [O II] SFRs, and Metallicities for the ASPECS-LP Line-search and Prior-based Sources at $z < 1.5$ with $S/N([\text{O II}]) > 3$

| ID | MUSE ID | z_{MUSE} | $F_{[\text{O II}] \lambda 3726 + \lambda 3729}$ ($\times 10^{-20} \text{ erg s}^{-1} \text{ cm}^{-2}$) | $F_{[\text{Ne III}] \lambda 3869}$ ($\times 10^{-20} \text{ erg s}^{-1} \text{ cm}^{-2}$) | $\text{SFR}_{[\text{O II}] \lambda 3726, 3729}^{\text{no dust}}$ ($M_{\odot} \text{ yr}^{-1}$) | $Z_{[\text{Ne III}]/[\text{O II}], \text{M08}}$ ($12 + \log(\text{O}/\text{H})$) |
|-----------|---------|-------------------|---|--|---|---|
| (1) | (2) | (3) | (4) | (5) | (6) | (7) |
| 3mm.06 | 8 | 1.0955 | 111.4 ± 1.4 | 1.9 ± 0.4 | 3.59 ± 0.05 | 9.05 ± 0.08 |
| 3mm.11 | 16 | 1.0965 | 24.4 ± 0.3 | 0.9 ± 0.1 | 0.79 ± 0.01 | 8.78 ± 0.06 |
| 3mm.14 | 924 | 1.0981 | 53.6 ± 1.6 | 2.4 ± 0.4 | 1.74 ± 0.05 | 8.70 ± 0.07 |
| 3mm.15 | 6870 | 1.0979 | 13.8 ± 0.4 | $< 0.2 \pm 0.1$ | ... | ... |
| 3mm.16 | 925 | 1.2942 | 67.0 ± 4.0 | $< 1.9 \pm 0.8$ | 3.26 ± 0.20 | $> 8.79 \pm 0.17$ |
| MP.3mm.01 | 985 | 1.0959 | 17.8 ± 1.5 | $< 0.6 \pm 0.5$ | 0.57 ± 0.05 | $> 8.56 \pm 0.29$ |
| MP.3mm.02 | 879 | 1.0874 | 245.9 ± 1.1 | 11.5 ± 0.6 | 7.78 ± 0.03 | 8.73 ± 0.02 |

Notes. (1) ASPECS-LP.3mm ID number. (2) MUSE ID (3) MUSE redshift. (4) [O II] $\lambda 3726 + \lambda 3729$ flux ($S/N > 3$). (5) [Ne III] $\lambda 3869$ flux (upper limits are reported if $S/N < 3$). (6) $\text{SFR}_{[\text{O II}] \lambda 3726, 3729}$ without correction for dust attenuation. (7) Metallicity from [Ne III]/[O II] based on Maiolino et al. (2008). We do not compute an $\text{SFR}_{[\text{O II}]}$ or metallicity for the X-ray detected AGN (3mm.15).

(e.g., Kewley et al. 2004). For all galaxies with $S/N([\text{O II}] \lambda 3726, 3729) > 3$, excluding the X-ray AGN, the [O II] $\lambda 3726 + \lambda 3729$ line flux measurements and SFRs are presented in Table 4.

4.2. Metallicities

It is well known that the gas-phase metallicity of galaxies is correlated with their stellar mass, with more massive galaxies having higher metallicities on average (e.g., Tremonti et al. 2004; Maiolino et al. 2008; Mannucci et al. 2010; Zahid et al. 2014). For the $1.0 < z < 1.42$ subsample, we have access to [Ne III] $\lambda 3869$, which allows us to derive a metallicity from [Ne III] $\lambda 3869$ /[O II] $\lambda 3726, 3729$. We follow the relation as presented by Maiolino et al. (2008), who calibrated the [Ne III]/[O II] line ratio against metallicities inferred from the direct T_e method (at low metallicity; $12 + \log \text{O}/\text{H} < 8.35$)

and theoretical models from Kewley & Dopita (2002; at high metallicity, mainly relevant for this paper; $12 + \log \text{O}/\text{H} > 8.35$). Since the wavelengths of [Ne III] $\lambda 3869$ and [O II] $\lambda 3726, 3729$ are close, this ratio is practically insensitive to dust attenuation. The physical underpinning lies in the fact that the ratio of the low-ionization [O II] and high-ionization [Ne III] lines is a solid tracer of the shape of the ionization field, given that neon closely tracks the oxygen abundance (e.g., Ali et al. 1991; Levesque & Richardson 2014; Feltre et al. 2018). As the ionization parameter decreases with increasing stellar metallicity (Dopita et al. 2006a, 2006b) and the metallicity of the young ionizing stars and their birth clouds is correlated, the ratio of [Ne III] $\lambda 3869$ /[O II] $\lambda 3726, 3729$ is a reasonable gas-phase metallicity diagnostic, albeit indirect, with significant scatter (Nagao et al. 2006; Maiolino et al. 2008) and sensitive to model assumptions (e.g., Levesque & Richardson 2014). If

Table 5
Molecular Gas Properties of the ASPECS-LP Line-search and Prior-based Sources, with Formal Uncertainties

| ID | z_{CO} | J_{up} | FWHM | F_{line} | L'_{line} | $L'_{\text{CO}(1-0)}$ | M_{mol} | M_{mol}/M_{\star} | t_{depl} |
|-----------|-----------------|-----------------|-----------------------|--------------------------|--|---|--------------------------------|----------------------------|-------------------|
| (1) | (2) | (3) | (km s ⁻¹) | (Jy km s ⁻¹) | ($\times 10^9$ K km s ⁻¹ pc ²) | ($\times 10^{10}$ K km s ⁻¹ pc ²) | ($\times 10^{10} M_{\odot}$) | (9) | (Gyr) |
| | | | (4) | (5) | (6) | (7) | (8) | (9) | (10) |
| 3mm.01 | 2.5436 | 3 | 517 ± 21 | 1.02 ± 0.04 | 33.9 ± 1.3 | 80.8 ± 13.8 | 29.1 ± 5.0 | 12.1 ± 2.1 | 1.2 ± 0.2 |
| 3mm.02 | 1.3167 | 2 | 277 ± 26 | 0.47 ± 0.04 | 10.7 ± 0.9 | 14.1 ± 2.1 | 5.1 ± 0.7 | 0.3 ± 0.1 | 4.5 ± 0.8 |
| 3mm.03 | 2.4534 | 3 | 368 ± 37 | 0.41 ± 0.04 | 12.8 ± 1.3 | 30.5 ± 5.9 | 11.0 ± 2.1 | 2.2 ± 0.6 | 1.6 ± 0.6 |
| 3mm.04 | 1.4140 | 2 | 498 ± 47 | 0.89 ± 0.07 | 23.2 ± 1.8 | 30.5 ± 4.3 | 11.0 ± 1.6 | 0.6 ± 0.1 | 1.8 ± 0.3 |
| 3mm.05 | 1.5504 | 2 | 617 ± 58 | 0.66 ± 0.06 | 20.4 ± 1.9 | 26.9 ± 4.0 | 9.7 ± 1.4 | 0.3 ± 0.1 | 1.6 ± 0.4 |
| 3mm.06 | 1.0951 | 2 | 307 ± 33 | 0.48 ± 0.06 | 7.7 ± 1.0 | 10.1 ± 1.7 | 3.6 ± 0.6 | 1.0 ± 0.2 | 1.1 ± 0.2 |
| 3mm.07 | 2.6961 | 3 | 609 ± 73 | 0.76 ± 0.09 | 27.9 ± 3.3 | 66.5 ± 13.6 | 23.9 ± 4.9 | 2.0 ± 0.5 | 1.3 ± 0.3 |
| 3mm.08 | 1.3821 | 2 | 50 ± 8 | 0.16 ± 0.03 | 4.0 ± 0.7 | 5.3 ± 1.2 | 1.9 ± 0.4 | 0.4 ± 0.1 | 0.5 ± 0.2 |
| 3mm.09 | 2.6977 | 3 | 174 ± 17 | 0.40 ± 0.04 | 14.7 ± 1.5 | 35.0 ± 6.8 | 12.6 ± 2.5 | 1.0 ± 0.2 | 0.4 ± 0.1 |
| 3mm.10 | 1.0367 | 2 | 460 ± 49 | 0.59 ± 0.07 | 8.5 ± 1.0 | 11.1 ± 1.9 | 4.0 ± 0.7 | 0.3 ± 0.1 | 2.2 ± 0.4 |
| 3mm.11 | 1.0964 | 2 | 40 ± 12 | 0.16 ± 0.03 | 2.6 ± 0.5 | 3.4 ± 0.7 | 1.2 ± 0.3 | 0.8 ± 0.2 | 1.2 ± 0.3 |
| 3mm.12 | 2.5739 | 3 | 251 ± 40 | 0.14 ± 0.02 | 4.8 ± 0.7 | 11.3 ± 2.5 | 4.1 ± 0.9 | 0.9 ± 0.2 | 1.3 ± 0.5 |
| 3mm.13 | 3.6008 | 4 | 360 ± 49 | 0.13 ± 0.02 | 4.3 ± 0.7 | 13.9 ± 3.4 | 5.0 ± 1.2 | 8.8 ± 2.8 | 1.2 ± 0.5 |
| 3mm.14 | 1.0981 | 2 | 355 ± 52 | 0.35 ± 0.05 | 5.6 ± 0.8 | 7.4 ± 1.4 | 2.7 ± 0.5 | 0.7 ± 0.1 | 1.0 ± 0.2 |
| 3mm.15 | 1.0964 | 2 | 260 ± 39 | 0.21 ± 0.03 | 3.4 ± 0.5 | 4.4 ± 0.8 | 1.6 ± 0.3 | 3.2 ± 1.1 | 0.3 ± 0.1 |
| 3mm.16 | 1.2938 | 2 | 125 ± 28 | 0.08 ± 0.01 | 1.8 ± 0.2 | 2.3 ± 0.4 | 0.8 ± 0.1 | 0.4 ± 0.1 | 0.7 ± 0.2 |
| MP.3mm.01 | 1.0962 | 2 | 169 ± 21 | 0.13 ± 0.03 | 2.1 ± 0.5 | 2.8 ± 0.7 | 1.0 ± 0.2 | 0.7 ± 0.2 | 1.3 ± 0.5 |
| MP.3mm.02 | 1.0872 | 2 | 107 ± 30 | 0.10 ± 0.03 | 1.6 ± 0.4 | 2.0 ± 0.6 | 0.7 ± 0.2 | 0.3 ± 0.1 | 0.3 ± 0.1 |

Note. The CO full width at half maximum (FWHM) and line fluxes are taken from Gonzalez-Lopez et al. (2019). (1) ASPECS-LP ID number. (2) CO redshift. (3) Upper level of CO transition. (4) CO line FWHM. (5) Integrated line flux. (6) Line luminosity. (7) CO(1–0) line luminosity assuming Daddi et al. (2015) excitation (Section 4.3). (8) Molecular gas mass assuming $\alpha_{\text{CO}} = 3.6$ K (km s⁻¹ pc²)⁻¹. (9) Molecular-to-stellar mass ratio, M_{mol}/M_{\star} . (10) Depletion time, $t_{\text{depl}} = M_{\text{mol}}/\text{SFR}$.

an AGN contributes significantly to the ionizing spectrum, the emission lines may no longer only trace the properties associated with massive star formation. For this reason, we exclude the sources with an X-ray AGN from the analysis of the metallicity.

We report the [Ne III] flux measurements and [Ne III]/[O II] metallicities in Table 4. The solar metallicity is $12 + \log \text{O}/\text{H} = 8.76 \pm 0.07$ (Caffau et al. 2011).

4.3. Molecular Gas Properties

The derivation of the molecular gas properties of our sources is detailed in Aravena et al. (2019). For reference, we provide a brief summary here.

We convert the observed CO($J \rightarrow J - 1$) flux to a molecular gas mass (M_{mol}) using the relations from Carilli & Walter (2013). To convert the higher-order CO transitions to CO(1–0), we need to know the excitation dependent intensity ratio between the CO lines, r_{J1} . We use the excitation ladder as estimated by Daddi et al. (2015) for galaxies on the MS, where $r_{21} = 0.76 \pm 0.09$, $r_{31} = 0.42 \pm 0.07$, and $r_{41} = 0.31 \pm 0.06$ (see also Decarli et al. 2016). To subsequently convert the CO(1–0) luminosity to M_{mol} , we use an $\alpha_{\text{CO}} = 3.6 M_{\odot}$ (K km s⁻¹ pc²)⁻¹, appropriate for star-forming galaxies (Daddi et al. 2010; see Bolatto et al. 2013 for a review). This choice of α_{CO} is supported by our finding that the ASPECS-LP sources are mostly on the MS and have (near-)solar metallicity (see Section 5.4).

With these conversions in mind, the molecular gas mass and derived quantities we report here can easily be rescaled to different assumptions following: $M_{\text{mol}}/M_{\odot} = (\alpha_{\text{CO}}/r_{J1})L'_{\text{CO}(J \rightarrow J-1)}/(\text{K km s}^{-1} \text{ pc}^2)$. The CO line and derived molecular gas properties are all presented in Table 5.

5. Results: Global Sample Properties

In this section we discuss the physical properties of all the ASPECS-LP sources that were found in the line search (without preselection) and based on a MUSE redshift prior. Since the sensitivity of ASPECS-LP varies with redshift, we discuss the galaxies detected in different CO transitions separately. In terms of the demographics of the ASPECS-LP detections, we focus on CO(2–1) and CO(3–2), where we have the most detections.

5.1. Stellar Mass and SFR Distributions

The majority of the detections consist of CO(2–1) and CO(3–2), at $1 < z < 2$ and $2 < z < 3$, respectively. A key question is in what part of the galaxy population we detect the largest gas-reservoirs at these redshifts.

We show histograms of the stellar masses and SFRs for the sources detected in CO(2–1) and CO(3–2) in Figure 6. We compare these to the distribution of all galaxies in the field that have a spectroscopic redshift from MUSE and our extended (photometric) catalog of all other galaxies. In the top part of each panel we show the percentage of galaxies we detect in ASPECS, compared to the number of galaxies in reference catalogs.

We focus first on the SFRs, shown in the right panels of Figure 6. The galaxies in which we detect molecular gas are the galaxies with the highest SFRs and the detection fraction increases with SFR. This is expected as molecular gas is a prerequisite for star formation and the most highly star-forming galaxies are thought to host the most massive gas reservoirs. The detections from the line search at $1.0 < z < 1.7$ alone account for $\approx 40\%$ of the galaxy population at $10 < \text{SFR}[M_{\odot} \text{ yr}^{-1}] < 30$, increasing to $> 75\%$ at $\text{SFR} > 30 M_{\odot} \text{ yr}^{-1}$. Including the prior-based detections, we find 60% of the population at

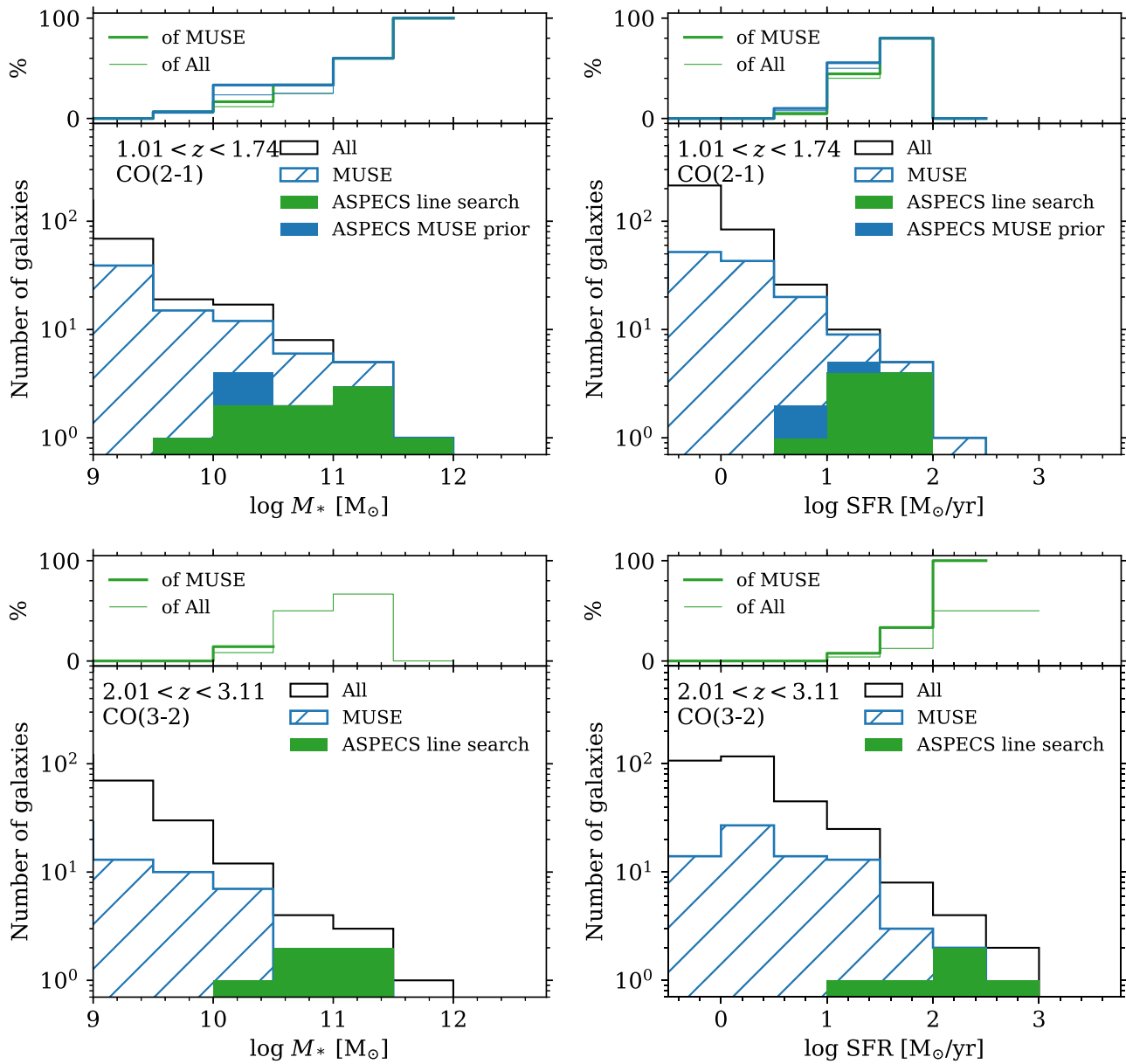


Figure 6. Histograms of the stellar mass (M_* , left) and star formation rate (SFR, right) of the ASPECS-LP detected galaxies, in comparison to all galaxies with MUSE redshifts and our extended photometric redshift catalog, in the indicated redshift range. We only show the range relevant to the ASPECS-LP detections: $M_* > 10^9 M_\odot$ and $\text{SFR} > 0.3 M_\odot \text{ yr}^{-1}$. Top: CO(2–1) detected sources at $1.01 < z < 1.74$. Bottom: CO(3–2) detected sources at $2.01 < z < 3.11$. In each of the four panels, the detected fraction in both reference catalogs is shown on top (no line is drawn if the catalog does not contain any objects in that bin). With the ASPECS-LP, we detect approximately 40% (50%) of all galaxies at $M_* > 10^{10} M_\odot$ ($> 10^{10.5} M_\odot$) at $1.0 < z < 1.7$ ($2.0 < z < 3.1$), respectively. In the same redshift bins, we detect approximately 60% (30%) of all galaxies with $\text{SFR} > 10 M_\odot \text{ yr}^{-1}$ ($> 30 M_\odot \text{ yr}^{-1}$).

$\text{SFR} \approx 20 M_\odot \text{ yr}^{-1}$. Similarly, at $2.0 < z < 3.1$, the detection fraction is highest in the most highly star-forming bin. Notably, however, with ASPECS-LP we probe molecular gas in galaxies down to much lower SFRs as well. The sources span over two orders of magnitude in SFR, from ≈ 5 to $> 500 M_\odot \text{ yr}^{-1}$.

The stellar masses of the ASPECS-LP detections in CO(2–1) and CO(3–2) are shown in the left panels of Figure 6. We detect molecular gas in galaxies spanning over two orders of magnitude in stellar mass, down to $\log M_* [M_\odot] \sim 9.5$. The completeness increases with stellar mass, which is presumably a consequence of the fact that more massive star-forming galaxies also have a larger gas fraction and higher SFR. At $M_* > 10^{10} M_\odot$, we are $\approx 40\%$ complete at $1.0 < z < 1.7$, while we are $\approx 50\%$ complete at $M_* > 10^{10.5} M_\odot$ at

$2 < z < 3.1$. The full distribution includes both star-forming and passive galaxies, which would explain why we do not pick-up all galaxies at the highest stellar masses.

5.2. AGN Fraction

From the deepest X-ray data over the field we identify five AGN in the ASPECS-LP line search sample (see Table 3). Two of these are detected in CO(2–1); namely, ASPECS-LP.3mm.05 and ASPECS-LP.3mm.15. The remaining three X-ray AGN are ASPECS-LP.3mm.01, 3mm.09, and 3mm.12, detected in CO(3–2). The AGN fraction among the ASPECS-LP sources is thus $2/10 = 20\%$ at $1.0 < z < 1.7$ and $3/5 = 60\%$ at $2.0 < z < 3.1$ (note that including the MUSE-prior sources decreases the AGN fraction). If we consider the total

number of X-ray AGN over the field, we detect $2/6 = 30\%$ of the X-ray AGN at $1.0 < z < 1.7$ and $3/6 = 50\%$ at $2.0 < z < 3.1$, without preselection.

The comoving number density of AGN increases out to $z \approx 2-3$ (Hopkins et al. 2007). Using a volume limited sample out to $z \sim 0.7$ based on the Sloan Digital Sky Survey and *Chandra*, Haggard et al. (2010) showed that the AGN fraction increases with both stellar mass and redshift, from a few percent at $M_* \sim 10^{10.7} M_\odot$, up to 20% in their most massive bin ($M_* \sim 10^{11.8} M_\odot$). Closer in redshift to the ASPECS-LP sample, Wang et al. (2017) investigated the fraction of X-ray AGN in the GOODS fields and found that among massive galaxies, $M_* > 10^{10.6} M_\odot$, 5%–15% and 15%–50% host an X-ray AGN at $0.5 < z < 1.5$ and $1.5 < z < 2.5$, respectively. The AGN fractions found in ASPECS-LP are broadly consistent with these ranges given the limited numbers and considerable Poisson error.

Given the AGN fraction among the ASPECS-LP sources (20% at $z \sim 1.4$ and 60% at $z \sim 2.6$), the question arises of whether we detect the galaxies in CO because they are AGN (i.e., AGN-powered), or, whether we detect a population of galaxies that hosts a larger fraction of AGN (e.g., because the higher gas content fuels both the AGN and star formation)? The CO ladders in, e.g., quasar host galaxies can be significantly excited, leading to an increased luminosity in the high- J CO transitions compared to star-forming galaxies at lower excitation (see, e.g., Carilli & Walter 2013; Rosenberg et al. 2015). With the band 3 data we are sensitive to the lower- J transitions, decreasing the magnitude of such a bias toward AGN. At the same time, the ASPECS-LP is sensitive to the galaxies with the largest molecular gas reservoirs, which are typically the galaxies with the highest stellar masses and/or SFRs. As AGN are more common in massive galaxies, it is natural to find a moderate fraction of AGN in the sample, increasing with redshift. Once the ASPECS-LP is complete with the observations of the band 6 (1 mm) data, we can investigate the higher J CO transitions for these sources and possibly test whether the CO is powered by AGN activity.

5.3. Obscured and Unobscured SFRs

We investigate the fraction of dust-obscured star formation by comparing the SFR derived from the [O II] $\lambda 3726, 3729$ emission line, without dust correction, with the (independent) total SFR from modeling the UV-FIR SED with MAGPHYS. We show the ratio between the SFR([O II]) and the total SFR(SED) as a function of the total SFR in Figure 7. We use the observed (unobscured) [O II] luminosity, yielding a measurement of the fraction of unobscured SFR. Immediately evident is the fact that more highly star-forming galaxies (which are on average more massive) are more strongly obscured. The median ratio (bootstrapped errors) of obscured/unobscured SFR is $10.8^{+3.0}_{-5.1}$ for the ASPECS-LP sources from the line search, which have a median mass of $10^{10.6} M_\odot$ (see $2.2^{+0.2}_{-0.1}$ for the complete sample of MUSE galaxies, with a median mass of $10^9 M_\odot$). Including the objects from the prior-based search does not significantly affect this fraction ($10.8^{+2.3}_{-5.1}$, at a median mass of $M_* \sim 10^{10.6} M_\odot$).

5.4. Metallicities at $1.0 < z < 1.42$

The molecular gas conversion factor is dependent on the metallicity, which is therefore an important quantity to constrain. Specifically, α_{CO} can be higher in galaxies with significantly subsolar metallicities, where a large fraction of the

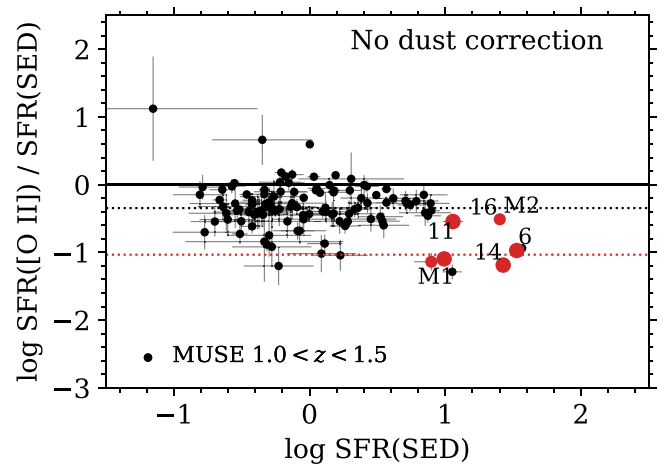


Figure 7. Total SFR from the SED fitting vs. the ratio between SFR ([O II] $\lambda 3726, 3729$) and SFR(SED) for the ASPECS-LP detected sources (red) and the MUSE $1.0 < z < 1.5$ reference sample (black). This shows the ratio between the unobscured SFR([O II]) and total SFR. The black and red dotted lines show the median ratio between SFR([O II]) and SFR(SED) for all galaxies and the ASPECS-LP sources only. The median fraction of obscured/unobscured SFR is $10.8^{+2.3}_{-5.1}$ for all the ASPECS-LP sources.

molecular gas may be CO faint, or lower in (luminous) starburst galaxies, where CO emission originates in a more highly excited molecular medium (e.g., Bolatto et al. 2013).

Given that the majority of the ASPECS-LP sources are reasonably massive, $M_* \geq 10^{10} M_\odot$, their metallicities are likely to be (super-)solar, based on the mass–metallicity relation (e.g., Zahid et al. 2014).

For the ASPECS-LP sources at $1.0 < z < 1.42$, the MUSE coverage includes [Ne III] $\lambda 3869$, which can be used as a metallicity indicator (Section 4.2). We infer a metallicity for ASPECS-LP.3mm.06, 3mm.11, and 3mm.14 and ASPECS-LP-MP.3mm.02. In addition, we can provide a lower limit on the metallicity for ASPECS-LP.3mm.16 and ASPECS-LP-MP.3mm.01, based on the upper limit on the flux of [Ne III].

In Figure 8, we show the ASPECS-LP sources on the stellar mass—gas-phase metallicity plane. For reference, we show the mass–metallicity relation from Maiolino et al. (2008; that matches the [Ne III]/[O II] calibration) and Zahid et al. (2014), both converted to the same IMF and metallicity scale (Kewley & Ellison 2008). The AGN-free ASPECS-LP sources span about half a dex in metallicity. They are all metal-rich and consistent with a solar or super-solar metallicity, in line with the expectations from the mass–metallicity relation.

The (near-)solar metallicity of our targets supports our choice of $\alpha_{\text{CO}} = 3.6 M_\odot (\text{K km s}^{-1} \text{pc}^2)^{-1}$, which was derived for $z \approx 1.5$ star-forming galaxies (Daddi et al. 2010) and is similar to the Galactic α_{CO} (see Bolatto et al. 2013).

6. Discussion

6.1. Sensitivity Limit to Molecular Gas Reservoirs

Being a flux-limited survey, the limiting molecular gas mass of the ASPECS-LP, $M_{\text{mol}}(z)$, increases with redshift. Based on the measured flux limit of the survey, we can gain insight into what masses of gas we are sensitive to at different redshifts. The sensitivity of the ASPECS-LP Band 3 data itself is presented and discussed in Gonzalez-Lopez et al. (2019): it is relatively constant across the frequency range, being deepest in the center where the different spectral tunings overlap.

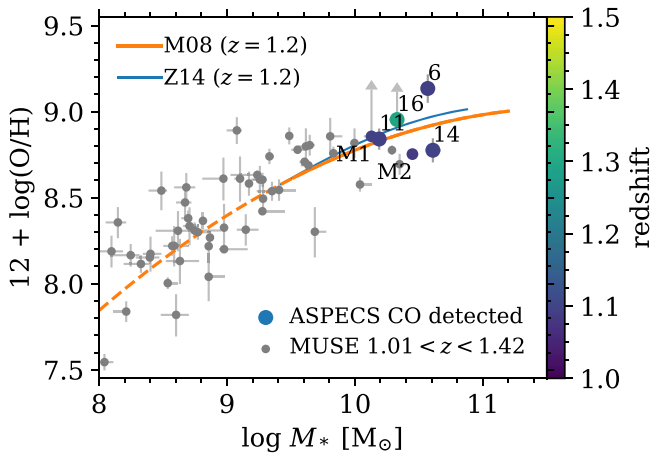


Figure 8. Stellar mass (M_*)–metallicity ($12 + \log \text{O}/\text{H}$) relation for the $1 < z < 1.5$ subsample. We use the ratio of $[\text{Ne III}] \lambda 3869$ and the $[\text{O II}] \lambda 3726, 3729$ -doublet, available at $z < 1.42$, to derive the metallicity (Maiolino et al. 2008). The solid lines show the mass–metallicity relations from Zahid et al. (2014) and Maiolino et al. (2008; converted to the same IMF and metallicity scale, Kewley & Ellison 2008), where the latter was interpolated to the average redshift of the sample (and extrapolated to lower masses; see the dashed line for reference). Overall, the ASPECS-LP galaxies are consistent with a (super-)solar metallicity.

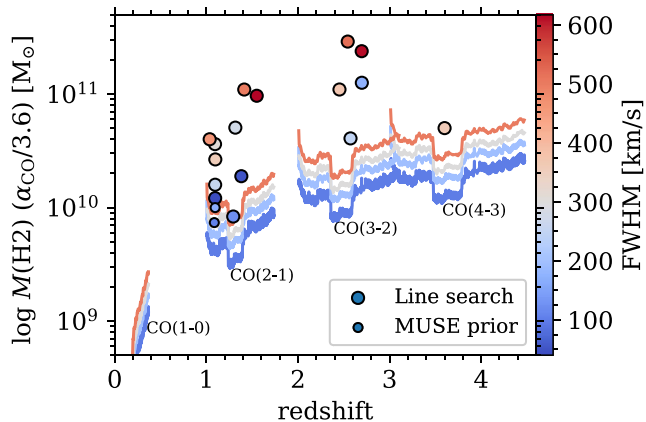


Figure 9. The 5σ molecular gas mass detection limit of ASPECS-LP as a function of redshift and CO line full width at half maximum (FWHM), assuming $\alpha_{\text{CO}} = 3.6$ and Daddi et al. (2015) excitation (see Section 4.3). The sensitivity varies with redshift and increases with the square root of the decreasing line width at fixed luminosity, indicated by the color. The points indicate the ASPECS-LP blind and prior-based sources, which are detected both in the deeper and shallower parts of the sensitivity curve.

Assuming a CO line full width at half maximum (FWHM) and an α_{CO} and excitation ladder as in Section 4.3, we can convert the root-mean-square noise level of ASPECS-LP in each channel to a sensitivity limit on $M_{\text{mol}}(z)$. The result of this is shown in Figure 9. With increasing luminosity distance, ASPECS-LP is sensitive to more massive reservoirs. This is partially compensated by the fact that the first few higher-order transitions are generally more luminous at the typical excitation conditions in star-forming galaxies. The $M_{\text{mol}}(z)$ function has a strong dependence on the FWHM, as broader lines at the same total flux are harder to detect (see also Gonzalez-Lopez et al. 2019). As the FWHM is related to the dynamical mass of the system, and we are sensitive to more massive systems at higher redshifts, these effects will conspire in further pushing up the gas-mass limit to more massive reservoirs.

At $1.0 < z < 1.7$, the lowest gas mass we can detect at 5σ (using the above assumptions and an FWHM for CO(2–1) of 100 km s^{-1}) is $M_{\text{mol}} \sim 10^{9.5} M_{\odot}$, with a median limiting gas mass over the entire redshift range of $M_{\text{mol}} \geq 10^{9.7} M_{\odot}$ ($M_{\text{mol}} \geq 10^{9.9} M_{\odot}$ at $\text{FWHM} = 300 \text{ km s}^{-1}$). At $2.0 < z < 3.1$ the median sensitivity increases to $M_{\text{mol}} \gtrsim 10^{10.3} M_{\odot}$, assuming an FWHM of 300 km s^{-1} for CO(3–2). In reality the assumptions made above can vary significantly for individual galaxies, depending on the physical conditions of their ISM.

As cold molecular gas precedes star formation, the $M_{\text{mol}}(z)$ selection function of ASPECS-LP can, to first order, be viewed as an $\text{SFR}(z)$ selection function. Since more massive star-forming galaxies have higher SFRs (albeit with significant scatter), a weaker correlation with stellar mass may also be expected. These rough, limiting relations will provide useful context to understand what galaxies we detect with ASPECS.

6.2. Molecular Gas across the Galaxy MS

We show the ASPECS-LP sources in the stellar mass–SFR plane at $1.01 < z < 1.74$ and $2.01 < z < 3.11$ in Figure 10. On average, star-forming galaxies with a higher stellar mass have a higher SFR, with the overall SFR increasing with redshift for a given mass, a relation usually denoted as the galaxy MS. We show the MS relations from Whitaker et al. (2014, W14) and Schreiber et al. (2015, S15) at the average redshift of the sample. The typical intrinsic scatter in the MS at the more massive end is around 0.3 dex or a factor of 2 (Speagle et al. 2014), which we can use to discern whether galaxies are on, above, or below the MS at a given mass.

6.2.1. Systematic Offsets in the MS

It is interesting to note that the average SFRs we derive with MAGPHYS are lower than what is predicted by the MS relationships from W14 and S15 (Figure 10). This offset is seen irrespective of including the FIR photometry to the SED fitting of the ASPECS-LP sources. This illustrates the fact that different methods of deriving SFRs from (almost) the same data can lead to somewhat different results (see, e.g., Davies et al. 2016 for a recent comparison). Both W14 and S15 derive their SFRs by summing the estimated UV and IR flux (UV+IR): W14 obtains the UV flux from integrating the UV part of their best-fit FAST SED (Kriek et al. 2009) and scales the *Spitzer*/MIPS $24 \mu\text{m}$ flux tot a total IR luminosity using a single template based on the Dale & Helou (2002) models. S15 instead uses (stacked) *Herschel*/PACS and SPIRE data for the IR luminosity, modeling these with Chary & Elbaz (2001) templates.

Recently, Leja et al. (2018) remodeled the UV– $24 \mu\text{m}$ photometry for all galaxies from the 3D-*HST* survey (which were used in deriving the W14 result) using the Bayesian SED fitting code PROSPECTOR- α (Leja et al. 2017). While PROSPECTOR- α also models the broadband SED in a Bayesian framework and shares several similarities with MAGPHYS, such as the energy-balance assumption, it is a completely independent code with its own unique features (e.g., the inclusion of emission lines, different stellar models, and nonparametric star formation histories). Interestingly, the SFRs derived by Leja et al. (2018) are ~ 0.1 – 1 dex lower than those derived from UV+IR, because of the contribution of old stars to the overall energy output that is neglected in $\text{SFR}(\text{UV}+\text{IR})$.

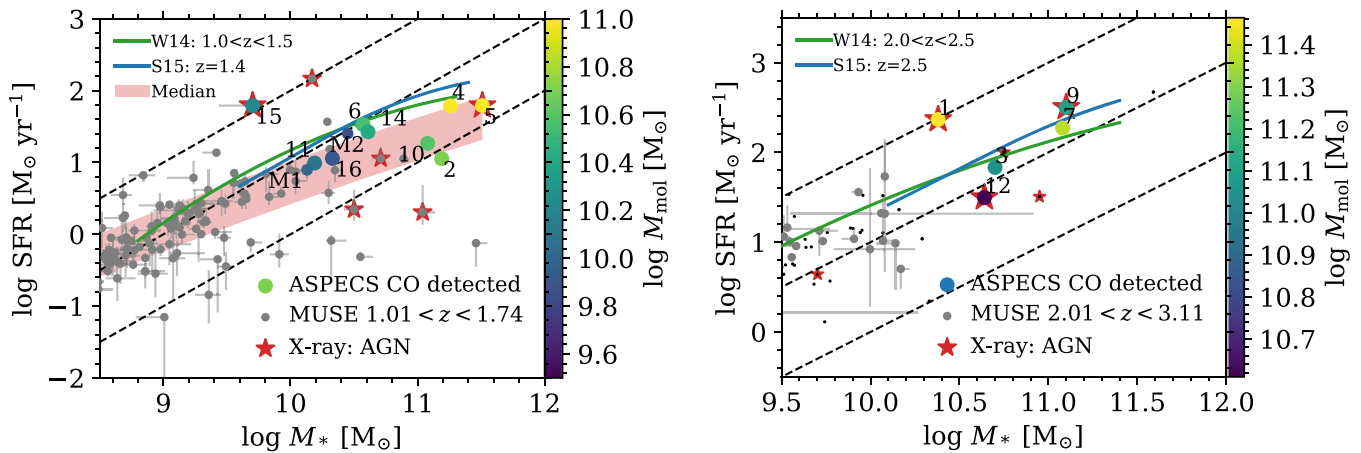


Figure 10. Stellar mass (M_*) vs. SFR (from MAGPHYS) for the CO(2–1) and CO(3–2) detected galaxies at $1.0 < z < 1.7$ (left) and $2.0 < z < 3.1$ (right), respectively. The ASPECS-LP line search and MUSE prior-based CO detections are represented by the larger and smaller circles respectively, colored by their molecular gas mass (M_{mol}). The gray and black points show the MUSE and photometric reference sample of galaxies, respectively. Red stars indicate X-ray sources identified as AGN from Luo et al. (2017). The green and blue solid curves denote the galaxy main-sequence relationships from, respectively, Whitaker et al. (2014) and Schreiber et al. (2015). The red band shows ± 0.3 dex around a polynomial fit to the running median of all galaxies in the panel. Lines of constant sSFR (0.1, 1, and 10 Gyr^{-1}) are shown black and dashed. At $z \sim 1.4$ ASPECS-LP detects molecular gas in galaxies that span a range of SFRs above, on, and below the galaxy MS.

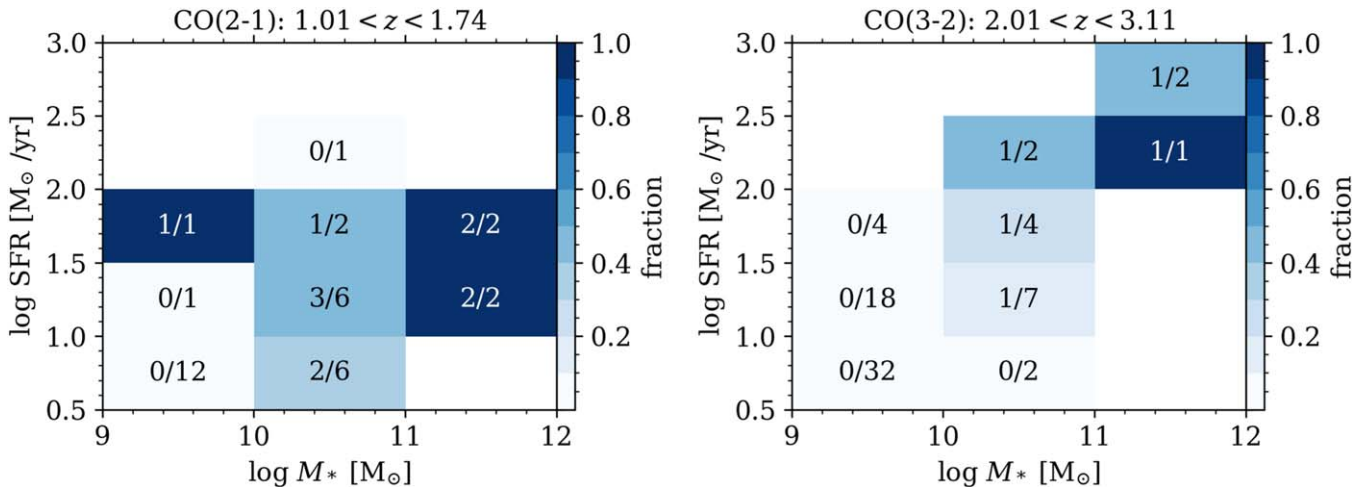


Figure 11. Fraction of sources detected by ASPECS-LP in M_* -SFR space at $1.01 < z < 1.74$ (left) and $2.01 < z < 3.11$ (right). This includes the detections from both the line search and the MUSE prior-based search. We are most complete at the highest SFRs and stellar masses. At a fixed stellar mass (SFR), the completeness fraction increases with SFR (stellar mass).

While the exact nature of this offset remains to be determined, solving the systematic calibrations between different SFR indicators (or a rederivation of the MS relationship) is beyond the scope of this paper. In the following we show ± 0.3 dex scatter around a second-order polynomial fit to the rolling median of the SFRs of all the galaxies (without any color selection) as a reference in the lower redshift bin. At the massive end where our ASPECS-LP sources lie, we indeed find that this curve lies somewhat below the W14 and S15 relationships. In the higher redshift bin the situation is less clear (given the limited number of sources) and we keep the literature references. With this description of the median SFR at a given stellar mass in hand, we are in the position to compare the SFRs of the individual ASPECS-LP sources to the population average SFR.

6.2.2. Normal Galaxies at $1.01 < z < 1.74$

The ASPECS-LP sources at $1.01 < z < 1.74$ are shown in the (M_*, SFR) -plane in the left panel of Figure 10. For

comparison we show all sources in this redshift range with a secure spectroscopic redshift, as MUSE is mostly complete for massive, star-forming galaxies in the regime of the ASPECS-LP detections at these redshifts (see Figure 6).

At the depth of the ASPECS-LP, we are sensitive enough to probe molecular gas reservoirs in a variety of galaxies that lie on and even below the MS at $z \sim 1.4$. Most of the ASPECS-LP galaxies detected in this redshift range lie on the MS, spanning a mass range of ~ 2 decades at the massive end. These galaxies belong to the population of normal star-forming galaxies at these redshifts.

As expected, with the primary sample alone we detect essentially all massive galaxies that lie above the MS, for $M_* > 10^{9.5} M_\odot$. The lowest mass galaxy we detect is ASPECS-LP.3mm.15, which is elevated significantly above the MS and is also an X-ray classified AGN. One galaxy, with the highest SFR of all, is a notable outlier for not being detected: MUSE#872 ($M_* = 10^{10.2} M_\odot$, $\text{SFR} \sim 150 M_\odot \text{yr}^{-1}$). From the prior-based search we find that no molecular gas emission is seen in this

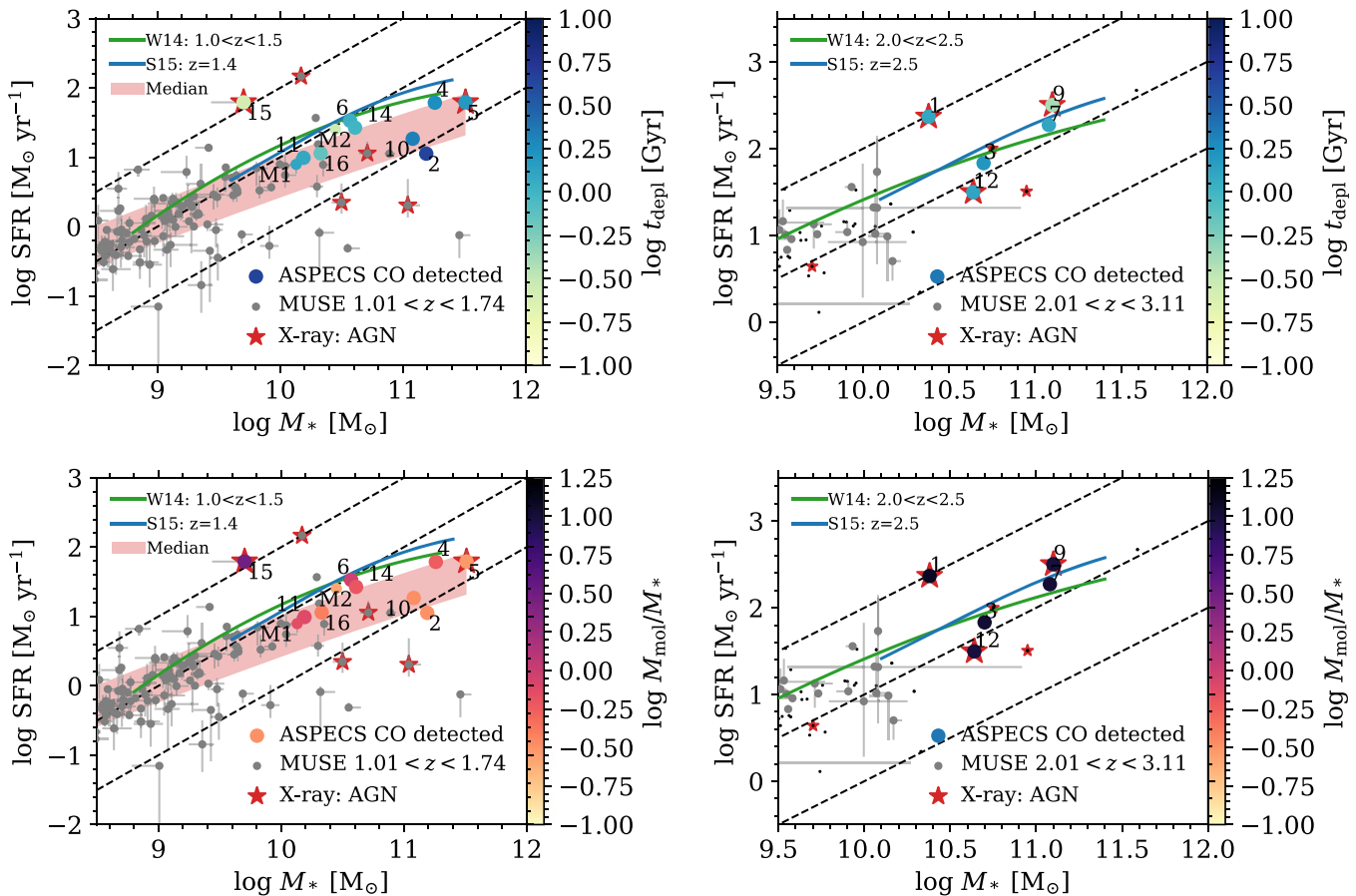


Figure 12. Stellar mass (M_*) vs. SFR for the galaxies at $1 < z < 1.7$ (left) and $2 < z < 3.1$ (right). The ASPECS-LP detections from the full and prior-based search are represented by the larger and smaller circles respectively. The gray and black points show the MUSE and photometric reference samples of galaxies, respectively. Red stars indicate X-ray sources identified as AGN from Luo et al. (2017). The color in the different panels denotes the change in depletion time ($t_{\text{depl}} = M_{\text{mol}}/\text{SFR}$; top) and molecular-to-stellar mass ratio (M_{mol}/M_* ; bottom). The green and blue solid curves denote the MS relationships from, respectively, Whitaker et al. (2014) and Schreiber et al. (2015). The red band shows ± 0.3 dex around a polynomial fit to the running median of all galaxies in the panel. Lines of constant sSFR (0.1, 1, and 10 Gyr^{-1}) are shown black and dashed. The gas fraction and depletion time vary systematically in galaxies across the main sequence.

source at lower levels either. While the nondetection of this object is very interesting, we caution that this source is also a broad-line AGN in MUSE and it is possible that its SFR is overestimated.

Notably, we also detect a number of galaxies that lie significantly below the MS (e.g., ASPECS-LP.3mm.02), meaning they have SFRs well below the population average. Despite their low SFR, these sources host a significant gas reservoir and have a gas fraction that is in some cases similar to MS galaxies at their stellar mass. The detection of a significant molecular gas reservoir in these sources is interesting, as these sources would typically not be selected in targeted observations for molecular gas.

Overall, we detect the majority of the galaxies on the massive end of the MS at $1.0 < z < 1.7$ in CO. We show the detection rate in bins of stellar mass and SFR in the left panel of Figure 11. At an SFR $> 10 M_{\odot} \text{yr}^{-1}$, we detect $> 60\%$ of galaxies at all masses at these redshifts. If we focus on galaxies with $M_* > 10^{10} M_{\odot}$, we are $> 60\%$ complete down to $\log \text{SFR} [M_{\odot} \text{yr}^{-1}] > 0.5$, where we encompass all MS galaxies.

6.2.3. Massive Galaxies at $2.01 < z < 3.11$

At $2.01 < z < 3.11$, we are sensitive to CO(3–2) emission from massive gas reservoirs. We plot the galaxies detected in CO(3–2) on the MS in the right panel of Figure 10. For

completeness, we have added ASPECS-LP.3mm.12 to the figure as well, but caution that the photometry is blended with a lower redshift foreground source. As the number of spectroscopic redshifts from MUSE is more limited in this regime, we also include galaxies from our extended photometric redshift catalog as small black dots (indicating AGN with red stars).

The detections from ASPECS-LP make up most of the massive and highly star-forming galaxies at these redshifts. Based on their CO flux, the sources all have a molecular gas mass of $\geq 10^{10.5} M_{\odot}$ and correspondingly high molecular gas fractions $M_{\text{mol}}/M_* \geq 1.0$. Their SFRs differ by over an order of magnitude. ASPECS-LP.3mm.07 and 09 are both at $z \approx 2.697$ and lie on the MS with SFRs between 150 and 350 $M_{\odot} \text{yr}^{-1}$. In contrast, ASPECS-LP.3mm.03 has a lower SFR of $< 100 M_{\odot} \text{yr}^{-1}$. ASPECS-LP.3mm.01 has a very high gas fraction and SFR for its stellar mass and is also detected as an X-ray AGN.

We show the quantitative detection fraction for CO(3–2) at these redshifts in the right panel of Figure 11. Note that, as the area of the HUDF and the ASPECS-LP is small, there are relatively few massive galaxies in the field at these redshifts.

6.3. Evolution of Molecular Gas Content in Galaxies

We now provide a brief discussion of the evolution of the molecular gas properties (and the individual outliers) in the full ASPECS-LP sample of 18 sources, including the MUSE

prior-based sources, in the context of the MUSE-derived properties. A more detailed discussion of these results will be provided in Aravena et al. (2019).

From systematic surveys of the galaxy population at $z \approx 0$, we know that the molecular gas properties of galaxies vary across the MS (e.g., Saintonge et al. 2016, 2017). The same trends are unveiled in the ASPECS-LP sample out to $z \approx 3$. To reveal these trends more clearly, we show the MS plot colored by the depletion time ($t_{\text{depl}} = M_{\text{mol}}/\text{SFR}$) and gas fraction (indicated by M_{mol}/M_*) in Figure 12. The molecular gas mass and depletion time of the ASPECS-LP sources vary systematically across the MS. On average, galaxies above the MS have higher gas fractions and shorter depletion times than galaxies on the MS, while the contrary is true for galaxies below the MS (longer depletion times, smaller gas fractions).

At $z \sim 1.4$, the sources span about an order of magnitude in depletion time, from 0.3 to 5 Gyr, with a median depletion time of ≈ 1.2 Gyr. This is comparable to the average depletion times found in $z = 1\text{--}3$ star-forming galaxies (e.g., Daddi et al. 2010; Tacconi et al. 2013). ASPECS-LP.3mm.02, which appears to harbor a substantial gas reservoir while its SFR puts it significantly below the MS, has a correspondingly long depletion time of several gigayears. Although the numbers are more limited at higher redshifts, we see a similar variety in depletion times at $z \sim 2.6$, with a median depletion time of ≈ 1.3 Gyr. For galaxies of similar masses we do not find a strong evolution in the depletion time between the $z \sim 1.4$ and $z \sim 2.6$ bins.

The evolution of the gas fraction across the MS is clearly seen for the sources at $z \sim 1.4$. The lowest gas-mass fractions we find are of the order of 30%, while the galaxies with the highest gas fractions have about equal mass in stars and in molecular gas, with a median of $M_{\text{mol}}/M_* \approx 0.6$. These are comparable to the gas fractions found at similar redshifts (Daddi et al. 2010; Tacconi et al. 2013). The gas fractions at $z \sim 2.6$ are substantially higher than they are at lower redshift. ASPECS-LP.3mm.09 and 12 have substantial gas fractions close to unity, while both ASPECS-LP.3mm.03 and 07, have a molecular gas mass of about $\times 2$ their mass in stars (median $M_{\text{mol}}/M_* \approx 2.0$). ASPECS-LP.3mm.1, 3mm.13, and 3mm.15 are outliers in this picture, with a substantially higher gas fraction than the other sources. Both 3mm.01 and 3mm.15 are also starbursts with a high inferred SFR and show an X-ray detected AGN. This high SFR is consistent with the high gas fraction and a picture in which the large gas reservoir fuels a strong starburst, while some gas powers the AGN simultaneously. As may be expected given the flux-limited nature of the observations, the highest redshift source, ASPECS-LP.3mm.13, also has a substantial gas fraction ($M_{\text{mol}}/M_* = 8.8 \pm 2.8$). As a whole, Figure 12 reveals the strength of the ASPECS-LP probing the molecular gas across cosmic time without preselection.

7. Summary

In this paper we use two spectroscopic integral-field observations of the Hubble Ultra Deep Field, ALMA in the millimeter, and MUSE in the optical regime, to further our understanding of the properties of the galaxy population at the peak of cosmic star formation ($1 < z < 3$). We start with the line emitters identified from the ASPECS-LP Band 3 (3 mm) data without any preselection (Gonzalez-Lopez et al. 2019). By using the MUSE data, as well as the deep multiwavelength data

that is available for the HUDF, we find that all ALMA-selected sources are associated with a counterpart in the optical/near-IR imaging. The spectroscopic information from MUSE enables us to associate all ALMA line emitters with emission coming from rotational transitions of carbon monoxide (CO) that result in unique redshift identifications: We identify 10 line emitters as CO(2–1) at $1 < z < 2$, five as CO(3–2) at $2 < z < 3$ and one as CO(4–3) at $z = 3.6$. The line search done using the ALMA data is conservative, to avoid contamination by spurious sources in the very large 3 mm data cube (Gonzalez-Lopez et al. 2019). We therefore also use the MUSE data as a positional and redshift prior to push the detection limit of the ALMA data to greater depth and identify two additional CO emitters at $z < 2.9$, increasing the total number of ALMA line detections in the field to 18.

We present MUSE spectra of all CO-selected galaxies, and use the diagnostic emission lines covered by MUSE to constrain the physical properties of the ALMA line emitters. In particular, for galaxies with coverage of [O II] $\lambda 3727$ /[Ne III] $\lambda 3869$ at $z \leq 1.5$ in the MUSE data, we infer metallicities consistent with being (super-)solar, which motivates our choice of a Galactic conversion factor to transform CO luminosities to molecular (H_2) gas masses for these galaxies in this series of ASPECS-LP papers (Aravena et al. 2019; Decarli et al. 2019; Gonzalez-Lopez et al. 2019; Popping et al. 2019). We also compare the unobscured [O II] $\lambda 3727$ -derived SFRs of the galaxies to the total SFR derived from their SEDs with MAGPHYS and confirm that a number of them have high extinction in the rest-frame UV/optical regime.

Using the very deep *Chandra* imaging available for the HUDF, we determine an X-ray AGN fraction of 20% and 60% among the CO(2–1) and CO(3–2) emitters at $z \sim 1.4$ and $z \sim 2.6$, respectively, suggesting that we do not preferentially detect AGN at $z < 2$. A future analysis of the band 6 data from the ASPECS-LP will reveal if those sources hosting an AGN show higher CO excitation compared to those that do not.

We use the exquisite multiwavelength data available for the HUDF to derive basic physical parameters (such as stellar masses and SFRs) for all galaxies in the HUDF. We recover the MS of galaxies and show that most of our CO detections are located toward higher stellar masses and SFRs, consistent with expectations from earlier studies. However, being a CO-flux-limited survey, besides galaxies on or above the MS our ALMA data also reveal molecular gas reservoirs in galaxies below the MS at $z \sim 1.4$, down to SFRs of $\approx 5 M_\odot \text{ yr}^{-1}$ and stellar masses of $M_* \approx 10^{10} M_\odot$. At higher redshift, we detect massive and highly star-forming galaxies in molecular gas emission on and above the MS. With our ALMA spectral scan, for stellar masses $M_* \geq 10^{10}$ ($10^{10.5}$) M_\odot , we detect about 40% (50%) of all galaxies in the HUDF at $1 < z < 2$ ($2 < z < 3$). The ASPECS-LP galaxies span a wide range of gas fractions and depletion times, which vary with their location above, on, and below the galaxy MS.

The cross-matching of the integral-field spectroscopy from ALMA and MUSE has enabled us to perform an unparalleled study of the galaxy population at the peak of galaxy formation in the HUDF. Given the large range of redshifts covered by the ALMA spectral lines, key diagnostic lines in the UV/optical are only covered by the MUSE observations in specific redshift ranges. The launch of the *James Webb Space Telescope* will greatly expand the coverage of spectral lines that will help to

further constrain the physical properties of ALMA-detected galaxies in the HUDF.

We are grateful to the referee for providing a constructive report. L.A.B. wants to thank Madusha L.P. Gunawardhana for her help with PLATEFIT. Based on observations collected at the European Southern Observatory under ESO programme(s): 094.A-2089(B), 095.A-0010(A), 096.A-0045(A), and 096.A-0045(B). This paper makes use of the following ALMA data: ADS/JAO.ALMA#2016.1.00324.L. ALMA is a partnership of ESO (representing its member states), NSF (USA) and NINS (Japan), together with NRC (Canada), NSC (USA) and ASIAA (Taiwan), and KASI (Republic of Korea), in cooperation with the Republic of Chile. The Joint ALMA Observatory is operated by ESO, AUI/NRAO, and NAOJ. The National Radio Astronomy Observatory is a facility of the National Science Foundation operated under cooperative agreement by Associated Universities, Inc.

“Este trabajo contó con el apoyo de CONICYT+Programa de Astronomía+ Fondo CHINA-CONICYT” J.G-L. acknowledges partial support from ALMA-CONICYT project 31160033. F.E.B. acknowledges support from CONICYT grant Basal AFB-170002 (FEB), and the Ministry of Economy, Development, and Tourism’s Millennium Science Initiative through grant IC120009, awarded to The Millennium Institute of Astrophysics, MAS (FEB). J.B. acknowledges support by Fundação para a Ciência e a Tecnologia (FCT) through national funds (UID/FIS/04434/2013) and Investigador FCT contract IF/01654/2014/CP1215/CT0003., and by FEDER through COMPETE2020 (POCI-01-0145-FEDER-007672). T.D-S. acknowledges support from ALMA-CONY CIT project 31130005 and FONDECYT project 1151239. J.H. acknowledges support of the VIDJ research programme with project number 639.042.611, which is (partly) financed by the Netherlands Organization for Scientific Research (NWO). D.R. acknowledges support from the National Science Foundation under grant No. AST-1614213. I.R.S. acknowledges support from the ERC Advanced Grant DUSTYGAL (321334) and STFC (ST/P000541/1)

Work on GUAUSTRO has been funded by the Japanese MEXT scholarship and its Grant-in-Aid for Scientific Research (21244012, 24253003), the ERC advanced grant 339659-MUSICOS, European Union’s Horizon 2020 research and innovation programme under Marie Skłodowska-Curie grant agreement No. 721463 to the SUNDIAL ITN, and from the Spanish MINECO under grant No. AYA2016-76219-P.

Facilities: ALMA, VLT:Yepun.

Software: TOPCAT (Taylor 2005), GUAUSTRO (Akhlaghi & Ichikawa 2015), IPYTHON (Perez & Granger 2007), NUMPY (Van Der Walt et al. 2011), MATPLOTLIB (Hunter 2007), ASTROPY (The Astropy Collaboration et al. 2013; Price-Whelan et al. 2018).

Appendix A

Source Description and Redshift Identifications

ASPECS-LP.3mm.01: CO(3–2) at $z = 2.543$. The brightest CO line emitter in the field. It is a *Chandra*/X-ray detected AGN (Luo et al. 2017, #718) and was already found in the line search at 3 and 1 mm in CO(3–2), CO(7–6), and CO(8–7) and continuum in the ASPECS-Pilot (Walter et al. 2016; Decarli et al. 2016, 3mm.1, 1mm.1, 1mm.2; Aravena et al. 2016, C1) as well as at 1 and 5 cm continuum (Dunlop et al. 2017; Rujopakarn et al. 2016, UDF3). The MUSE spectrum

(MUSE#35) reveals a high S/N continuum with a wealth of UV absorption features and C III] $\lambda 1907, 1909$ emission, confirming the redshift (Figure 13). The source is a (likely interacting) pair with the source $\sim 1''.5$ to the west, MUSE#24, at the same redshift ($\Delta v \approx 76 \text{ km s}^{-1}$).

ASPECS-LP.3mm.02: CO(2–1) at $z = 1.317$. Detected in both [O II] and continuum in MUSE. This source is also detected in continuum at 1 mm and 5 cm (Rujopakarn et al. 2016; Dunlop et al. 2017, UDF16). [O II] $\lambda 3726$ is severely affected by a skyline complicating the redshift and line-flux measurement. We remeasure the cataloged redshift for this source, which is used to compute the velocity offset with CO(2–1) (Table 1). Since we cannot confidently recover the full [O II] flux, we do not include this source in the analyses of Sections 5.3 and 5.4.

ASPECS-LP.3mm.03: CO(3–2) at $z = 2.454$. Photometric redshift indicates $z = 2-3$ (Skelton et al. 2014; Rafelski et al. 2015), perfectly in agreement with the detection of CO(3–2) at $z = 2.45$. The source is faint ($m_{F775W} > 27$ mag) and an extraction of the MUSE spectrum yields essentially no continuum signal (see Figure 13). This supports a redshift solution between $z = 2-3$, where no bright emission lines lie in the MUSE spectral range (see Section 2.2). Beside there being little continuum in the spectrum, there are no spectral features (in particular emission lines) indicative of a lower redshift ([O II] at $z = 1.30$) or higher redshift ($\text{Ly}\alpha$ at $z = 3.60$) solution. Detected in continuum at 1 mm and 5 cm (Rujopakarn et al. 2016; Dunlop et al. 2017, UDF4).

ASPECS-LP.3mm.04: CO(2–1) at $z = 1.414$. MUSE spectrum shows [O II] and (weak) continuum. Detected in continuum at 1 mm and 5 cm (Rujopakarn et al. 2016; Dunlop et al. 2017, UDF6).

ASPECS-LP.3mm.05: CO(2–1) at $z = 1.550$. A massive ($M_* \approx 10^{11.5} M_\odot$) galaxy and an X-ray classified AGN (Luo et al. 2017, #748). It was also detected by the ASPECS-Pilot in 1 mm continuum (C2, Aravena et al. 2016; see Dunlop et al. 2017), in CO(2–1) and also CO(5–4) and CO(6–5) (ID.3, Decarli et al. 2016), and in 5 cm continuum (Rujopakarn et al. 2016, UDF8). NIR spectroscopy from the SINS survey (Förster Schreiber et al. 2009) reveals $\text{H}\alpha \lambda 6563$, confirming the redshift we also find from MUSE, based on the Fe II and Mg II absorption features.

ASPECS-LP.3mm.06: CO(2–1) at $z = 1.095$. Part of an overdensity in the HUDF at the same redshift. Rich star-forming spectrum in MUSE with a wealth of continuum and emission features. Detected in X-ray, but not classified as an AGN (Luo et al. 2017, #749).

ASPECS-LP.3mm.07: CO(3–2) at $z = 2.696$. Photometric redshift indicates $z = 2-3$ (Skelton et al. 2014; Rafelski et al. 2015), perfectly in agreement with the detection of CO(3–2) at $z = 2.69$. The source is faint ($m_{F775W} > 27$ mag) and a reextraction of the MUSE spectrum yields essentially no continuum signal (see Figure 14). This supports a redshift solution between $z = 2-3$, where no bright emission lines lie in the MUSE spectral range (see Section 2.2). Beside there being little continuum in the spectrum, there are no spectral features indicative of a lower redshift or higher redshift solution (see ASPECS-LP.3mm.03). There is reasonably close proximity between ASPECS-LP.3mm.07 and 09 at $z = 2.69$, which are separated by only $\sim 7''.5$ (60 kpc at that redshift). This object is one of the brightest sources in the HUDF at 1 mm (UDF2;

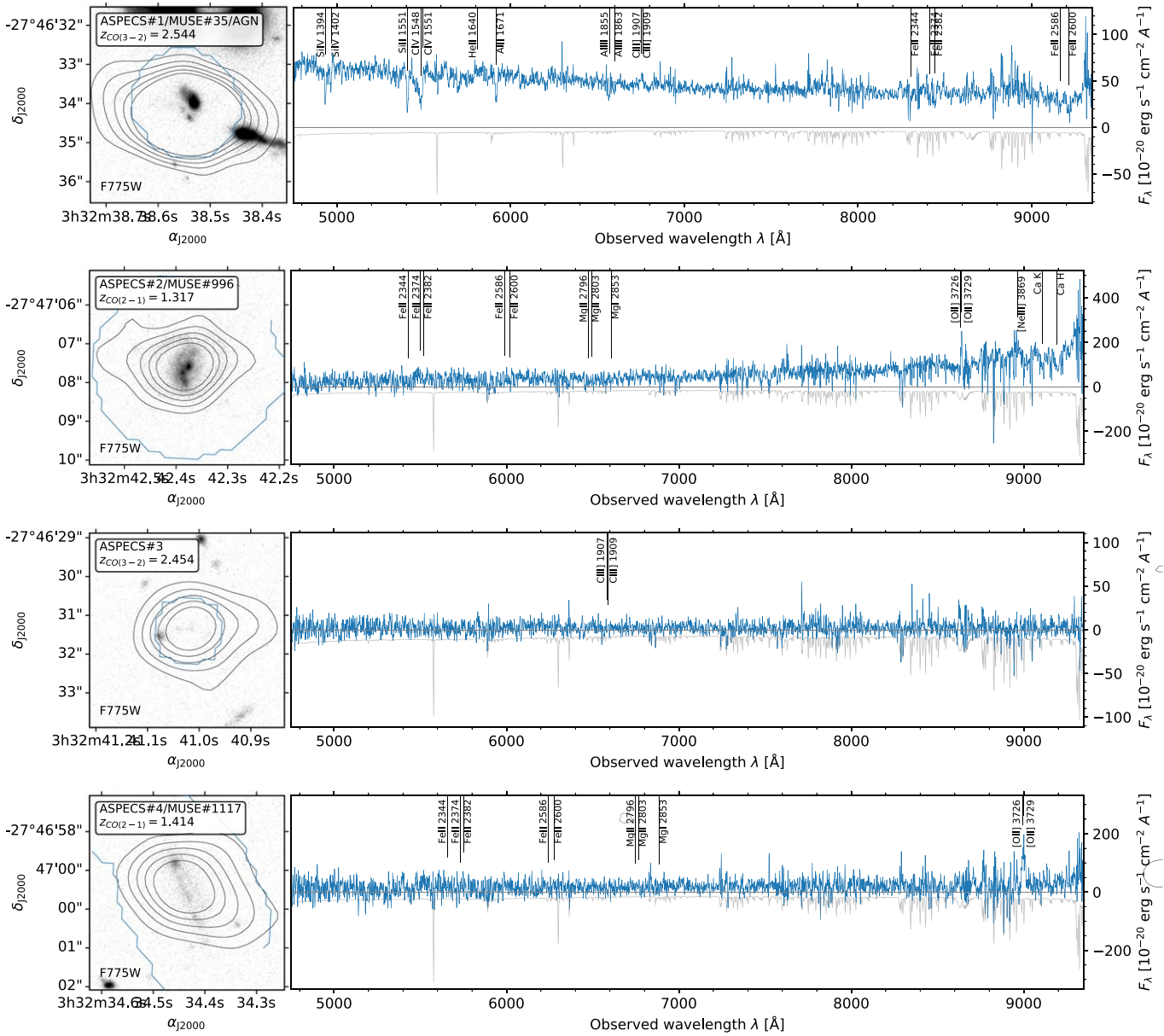


Figure 13. MUSE spectroscopy of the ASPECS-LP sources. Left: *HST*/F775W cutout. The colored contour(s) mark the region of the spectral extraction(s), defined by convolving the MUSE PSF with the *HST* segmentation map (see Inami et al. 2017 for details), or a fixed $0''.8$ aperture (in the case of a new extraction; #3, #7, #9, #13). The black contours indicate the CO emission from $\pm[3, \dots, 11]\sigma$ in steps of 2σ . Right: MUSE spectrum (1.5 \AA Gaussian smoothing) extracted over the marked region. The 1σ uncertainty on the spectrum is shown by the gray line in the direction of negative flux (for clarity), and is largest around skylines. The (expected) positions of different spectral features are annotated; this does not indicate that the feature is also detected. Spectra and lines of nearby or blended sources are shown in red.

Dunlop et al. 2017) and also detected at 5 cm (Rujopakarn et al. 2016).

ASPECS-LP.3mm.08: CO(2–1) at $z = 1.382$. The source has a more complex morphology, which was already discussed in the ASPECS-Pilot program (Decarli et al. 2016, see their Figure 3). The CO emission is spatially consistent with a system of spiral galaxies. MUSE reveals that the southwest spiral is in the foreground at $z = 1.087$. Careful examination of the MUSE cube reveals [O II] emission matching the CO redshift in an arc north of the galaxies and possibly toward the southwest, which is $\sim 1''.8$ away of peak of the CO emission ($\sim 15 \text{ kpc}$ at the redshift of the source). A potential scenario is that the northeast spiral galaxies are the background source, in which case the ionized gas emission of the spiral is completely

obscured by the disk of the (southwest) foreground spiral. This is consistent with the spatial position of the CO emission. An alternative scenario is that of a third disk galaxy harboring the CO reservoir, which is completely hidden from sight by the spiral galaxies in the foreground, except for the structures seen in the north and east. We note that resolved SED fitting of this source was recently performed by Sorba & Sawicki (2018), assuming the foreground redshift for the entire system. A clear break can be seen in the sSFR (their Figure 1). for the northern arm and possibly also a southwest arm; consistent with locations where [O II]-emission is seen. For the purpose of this paper, we associate the northeast spiral with ASPECS-LP.3mm.08 and the southwest spiral with ASPECS-LP-MP.3mm.02, but we note that this is uncertain in the case of

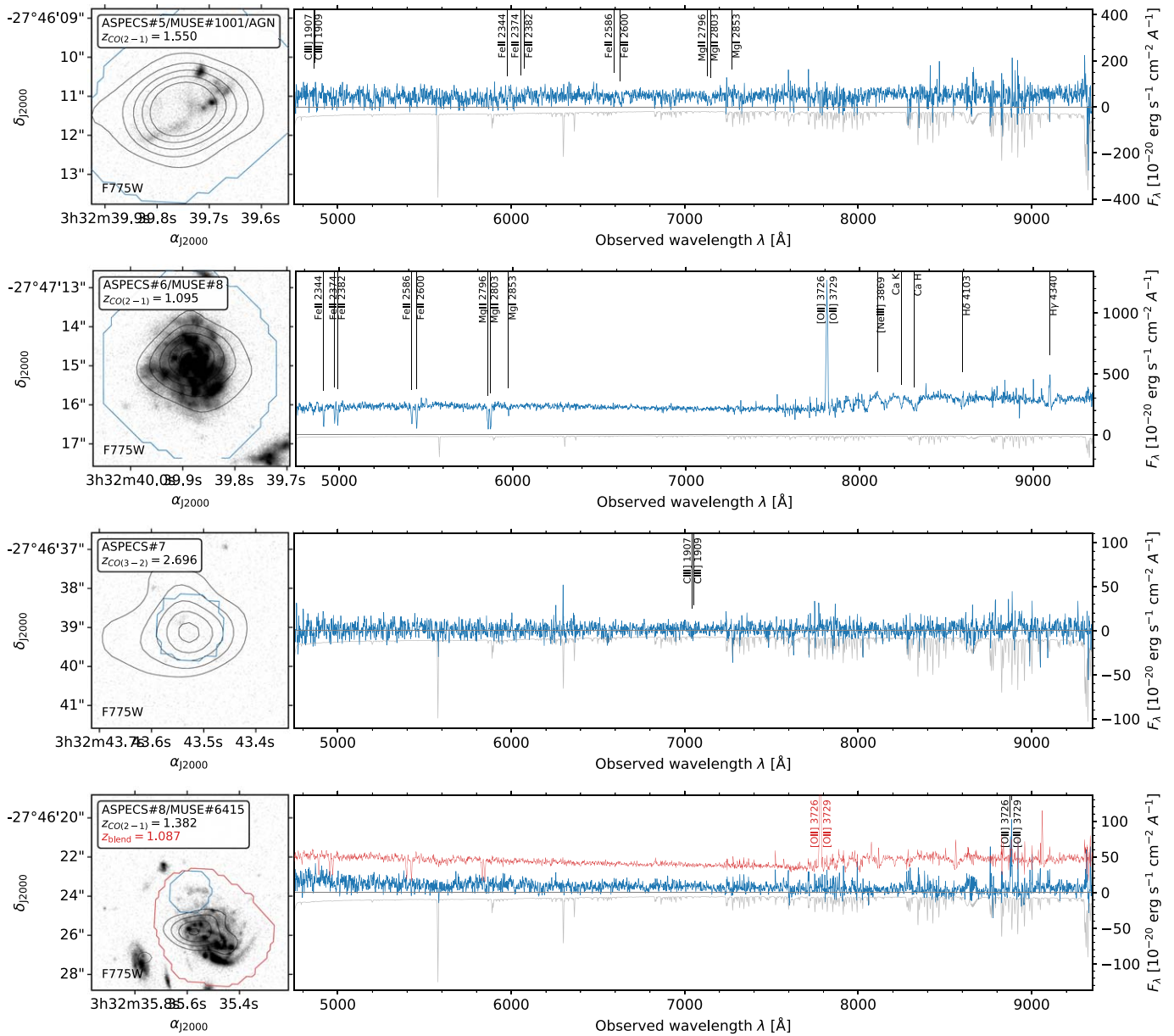


Figure 14. Continuation of Figure 13. We show spectrum of the complete system of spiral galaxies at ASPECS-LP.3mm.08 in red (scaled down by a factor of 10), to make the faint [O II] $\lambda 3726, 3729$ line matching the CO(2–1) redshift visible. The spectrum for ASPECS-LP.3mm.08 itself is shown in blue (extracted only over a part of the spiral arm). Note the foreground source is independently detected in CO(2–1) as ASPECS-LP-MP.3mm.02 and the fully annotated spectrum for this source is shown in Figure 15.

ASPECS-LP.3mm.08. Given the limited flux we observe from the ionized gas, we do not discuss this source in that context.

ASPECS-LP.3mm.09: CO(3–2) at $z = 2.698$. Photometric redshift indicates $z = 2-3$ (Skelton et al. 2014; Rafelski et al. 2015), perfectly in agreement with the detection of CO(3–2) at $z = 2.69$. The source is faint ($m_{F775W} > 27$ mag), yet, UV absorption features at $z = 2.695$, matching the expected redshift of CO(3–2) at $z = 2.698$, are found in the MUSE spectrum at the position of the source (see Figure 15). The features arise in a source (MUSE#6941) $\sim 0''.8$ to the north (~ 6.5 kpc at $z \sim 2.7$). The spectrum of the northern source reveals a superposition of the $z = 2.695$ source with a foreground galaxy at $z = 1.555$. This is also suggestive from the morphology in *HST*, which shows a redder central clump for the northern source. Given the potential proximity of the two sources, both spatially and spectrally, ASPECS-LP.3mm.09

could be part of a pair of galaxies with the source to the north. Notably, ASPECS-LP.3mm.09 is also detected as an X-ray AGN; (Luo et al. 2017, #865). Note that there is also reasonably close proximity between ASPECS-LP.3mm.07 and 09 at $z = 2.69$, which are separated by only $\sim 7''.5$ (60 kpc at that redshift). One of the brightest sources in the HUDF at 1 mm (UDF1; Dunlop et al. 2017), also detected at 5 cm (Rujopakarn et al. 2016).

ASPECS-LP.3mm.10: CO(2–1) at $z = 1.037$. The lowest redshift detection. Features a close star-forming companion at the same redshift. The MUSE spectrum shows continuum with both absorption and emission line features ([O II]). We reextract the spectrum with a new segmentation map to recompute the redshift and to minimize blending of the [O II] flux from the close companion at slightly different redshift. The [O II] line is detected in the source, but given the residual

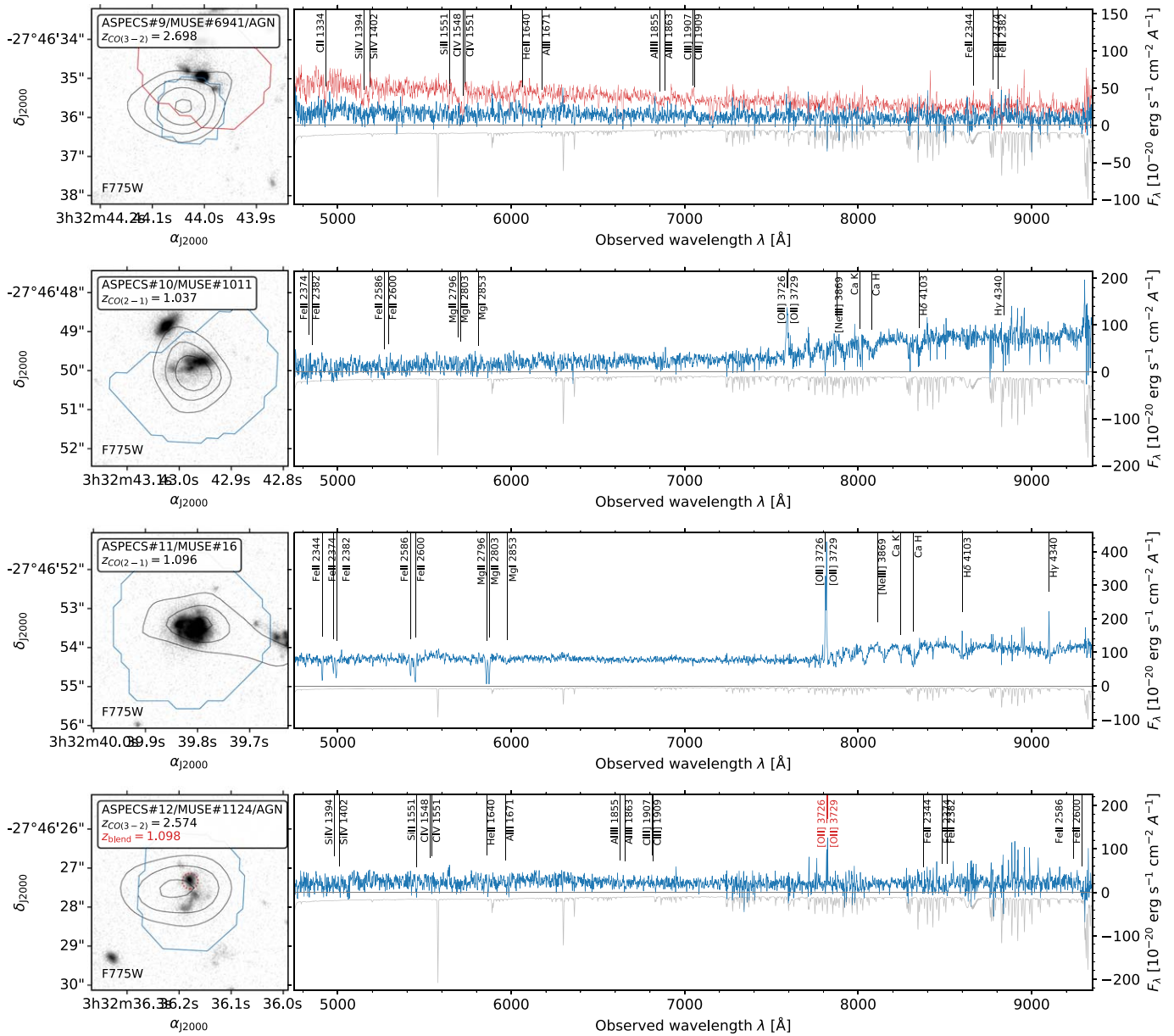


Figure 15. Continuation of Figure 13. For ASPECS-LP.3mm.09 the UV absorption features matching the CO(3–2) redshift are seen in the source to the north (red spectrum). ASPECS-LP.3mm.12 is blended with a foreground [O II]-emitter (see Figure 18).

deblending uncertainties we do not take into account in the analyses of Sections 5.3 and 5.4.

ASPECS-LP.3mm.11: CO(2–1) at $z = 1.096$. Part of the overdensity in the HUDF at the same redshift. MUSE reveals a rich star-forming spectrum with stellar continuum and both absorption and emission ([O II], [Ne III]) features.

ASPECS-LP.3mm.12: CO(3–2) at $z = 2.574$. Detected in 1 mm continuum (C4; Aravena et al. 2016) and an X-ray AGN (Luo et al. 2017, #680). The source contains a CO line at 96.76 GHz. The optical counterpart shows red colors in *HST* and features a blue component toward the north. The source is considered to be a single galaxy in most photometric catalogs (e.g., Skelton et al. 2014; Rafelski et al. 2015). However, the redshift from the MUSE catalog for this source, $z = 1.098$ (based on a confident [O II] detection, see Figure 15), is incompatible with being CO(2–1), which would be at $z = 1.383$. Closer inspection of the source in the MUSE IFU

data reveals that the [O II] emission is only originating from the blue clump to the north of the source (see Figure 18). A reanalysis of the MUSE spectrum revealed weak absorption features that, when cross-correlated with an absorption line template, correspond to a redshift of $z = 2.5738$. Assuming that the CO line is CO(3–2) instead, this independently matches the redshift from ASPECS-LP exactly ($z = 2.5738$). To further confirm that the absorption features are associated with ASPECS-LP.3mm.12, we spatially stacked narrow bands over all strong UV absorption features (without any preselection). To construct the narrow band, we sum the flux over each absorption feature (assuming a fixed 7 \AA line width) and subtract the continuum measured in two side bands offset by $\pm 10 \text{ \AA}$ (same width in total). We then stacked the individual narrow bands by summing the flux in each spatial pixel (note that the same result is found when taking the mean or median). The stacked absorption features have $S/N > 4$ and are

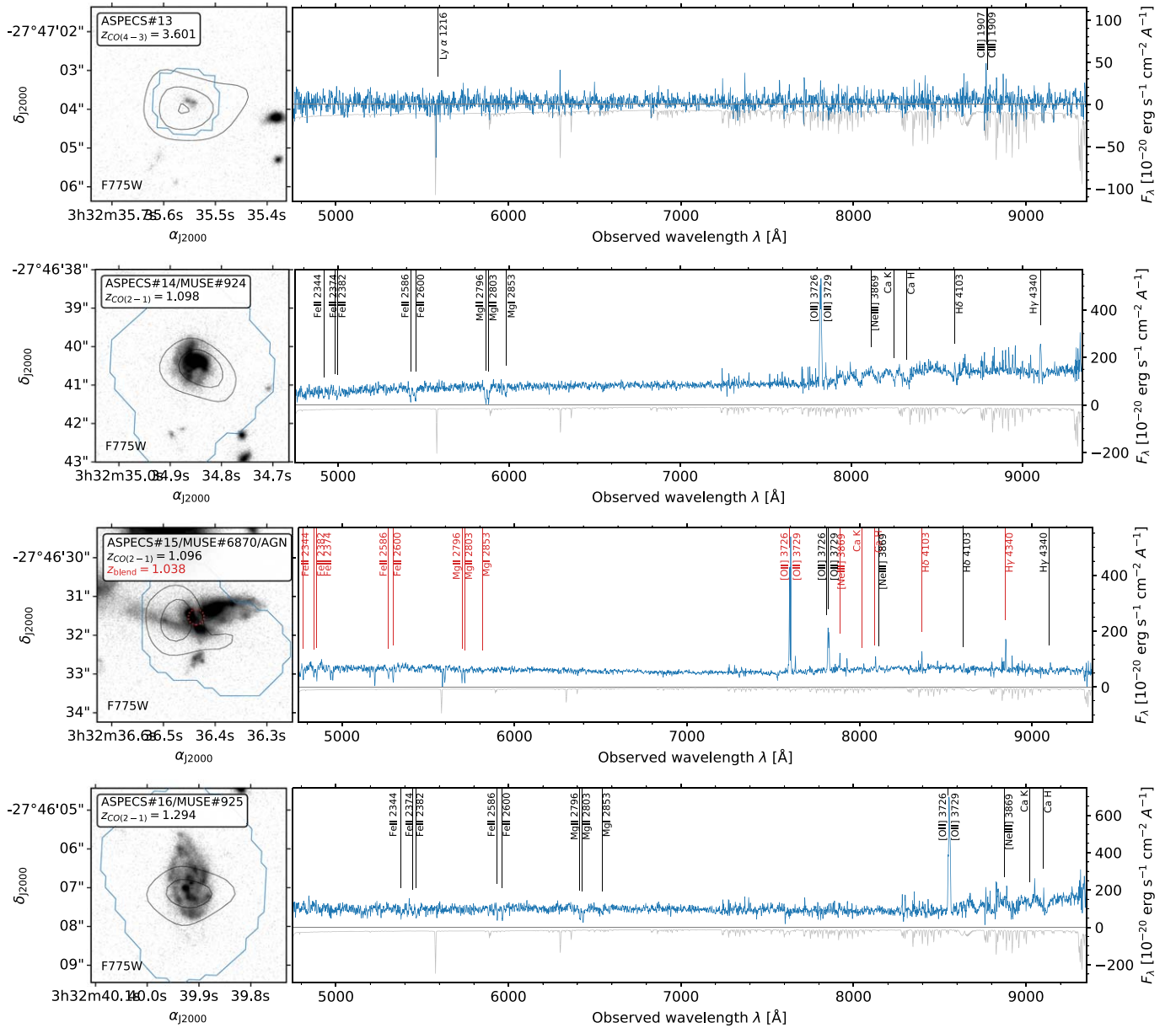


Figure 16. Continuation of Figure 13. The spectrum of ASPECS-LP.3mm.15 is severely blended. We have highlighted the strongest blended features (from a foreground source at $z = 1.038$) in red.

cospatial with the background galaxies and the CO, confirming the detection of CO(3–2) at $z = 2.5738$ (see Figure 18).

ASPECS-LP.3mm.13: CO(4–3) at $z = 3.601$. Highest redshift CO detection. It is an F435W dropout and the photometric redshifts for this source consistently suggest that it lies in the $z = 3–4$ range (Skelton et al. 2014; Straatman et al. 2016), with $z_{\text{BPZ}} = 3.67^{+0.74}_{-0.24}$ (Rafelski et al. 2015). These all suggest a detection of CO(4–3) at $z = 3.601$. In order to spectroscopically confirm this redshift, we extract a MUSE spectrum at the position of the source. The strongest UV emission line observed by MUSE at these redshifts is Ly α , while it also covers the much weaker C III] line. Both are not detected in the spectrum of ASPECS-LP.3mm.13. The nondetection of C III] at the 10 hr depth of the mosaic is understandable, as robustly detecting C III] at these redshifts is challenging (see Maseda et al. 2017 for an in-depth discussion, which finds the highest redshift detection of C III] in

the deep 30 hr MUSE data to be at $z \sim 2.9$). Unfortunately, at $z = 3.601$ the expected position of Ly α in MUSE falls close to the [O I] $\lambda 5577$ skyline (Figure 16), which could explain why it is not detected. Furthermore, the source is likely to have significant dust content in which case no Ly α emission may be expected at all. Nevertheless, while at $m_{\text{F775W}} = 26.4$, the spectrum does not reveal emission or absorption lines compatible with a solution for CO(2–1) at $z = 1.30$ or CO(3–2) at $z = 2.45$, which suggests that a higher redshift solution is appropriate for ASPECS-LP.3mm.13 (in agreement with the photo z). In summary, the combined evidence of the photometric redshifts indicating $z \sim 3.5$ and the lack of a lower redshift solution from MUSE makes the case for the detection of CO(4–3) at $z = 3.601$ in ASPECS-LP.3mm.13.

ASPECS-LP.3mm.14: CO(2–1) at $z = 1.098$. Part of an overdensity in the HUDF. MUSE reveals a rich spectrum with

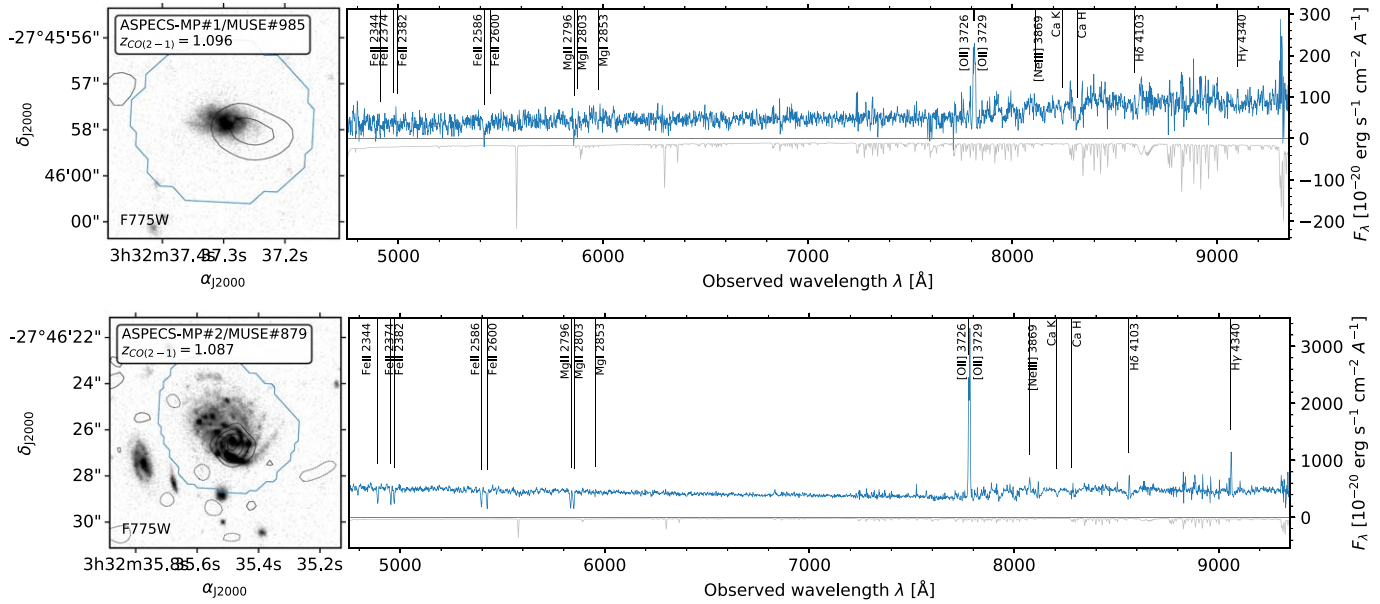


Figure 17. Continuation of Figure 13, showing the MUSE-prior-based sources.

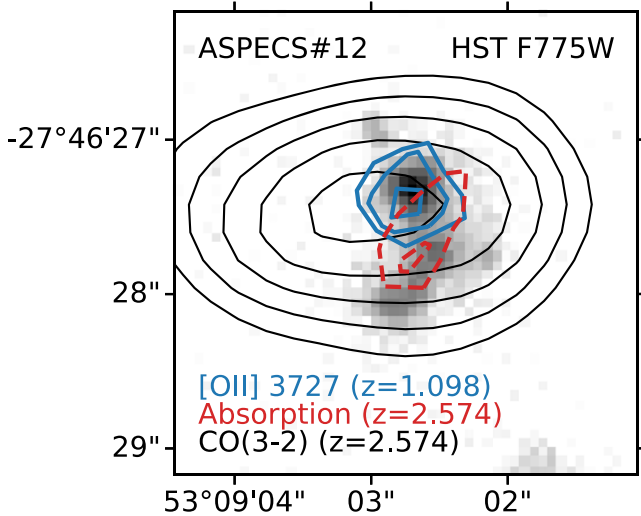


Figure 18. *HST*/F775W cutout of ASPECS-LP.3mm.12, with CO(3–2) emission at $z = 2.5738$. The MUSE spectrum of this source reveals two redshifts. There is [O II] emission at $z = 1.098$, spatially consistent with a foreground galaxy to the north. While the continuum is faint, cross-correlating the spectrum with an absorption line template reveals a peak at $z = 2.5738$ with $S/N > 4$. Subsequent stacking of the UV absorption lines (C II $\lambda 1334$, Si IV $\lambda 1394$, 1402, Si II $\lambda 1551$, C IV $\lambda 1548$, 1551, Al II $\lambda 1671$, and Al III $\lambda 1855$, 1863) reveals that the absorption is cospatial with the background galaxy and consistent with the redshift of CO(3–2). All contours start at $\pm 3\sigma$, increasing by 1σ (where solid and dashed lines indicate emission and absorption respectively).

continuum, absorption, and a range of emission lines (among which [O II], [Ne III] and Balmer lines).

ASPECS-LP.3mm.15: CO(2–1) at $z = 1.096$. Part of an overdensity in the HUDF at the same redshift. The source lies

in a very crowded part of the sky with multiple galaxies at different redshifts overlapping in projection. It was detected in X-rays, classified as AGN (Luo et al. 2017, #689). The source was also covered by the ASPECS-Pilot program and detected in CO(2–1) and CO(4–3) (Decarli et al. 2016, ID.5).

ASPECS-LP.3mm.16: CO(2–1) at $z = 1.294$ shows a disk-like morphology. MUSE spectrum reveals a stellar continuum with absorption, as well as emission lines ([O II] and [Ne III]).

ASPECS-LP-MP.3mm.01: CO(2–1) at $z = 1.096$. Part of an overdensity in the HUDF at the same redshift. MUSE spectrum shows stellar continuum with absorption, as well as emission lines ([O II]; Figure 17).

ASPECS-LP-MP.3mm.02: CO(2–1) at $z = 1.087$. Foreground galaxy to ASPECS-LP.3mm.08, also described in Decarli et al. (2016). See ASPECS-LP.3mm.08 for a further description.

Appendix B Magphys Fits for All CO-detected Galaxies

We perform SED fitting with MAGPHYS for all ASPECS-LP galaxies, as described in detail in Section 2.3. The following bands are considered in the SED fitting of the ASPECS-LP galaxies: U₃₈ (0.37 μm), IA₄₂₇ (0.43 μm), F435W (0.43 μm), B (0.46 μm), IA₅₀₅ (0.51 μm), IA₅₂₇ (0.53 μm), V (0.54 μm), IA₅₇₄ (0.58 μm), F606W (0.60 μm), IA₆₂₄ (0.62 μm), IA₆₇₉ (0.68 μm), IA₇₃₈ (0.74 μm), IA₇₆₇ (0.77 μm), F775W (0.77 μm), I (0.91 μm), F850LP (0.90 μm), J (1.24 μm), tJ (1.25 μm), F160W (1.54 μm), H (1.65 μm), tK_s (2.15 μm), K (2.21 μm), IRAC (3.6 μm , 4.5 μm , 5.8 μm , 8.0 μm), MIPS (24 μm), PACS (100 μm and 160 μm) and ALMA Band 6 (1.2 mm) and Band 3 (3.0 mm). The resulting SEDs are shown in Figure 19.

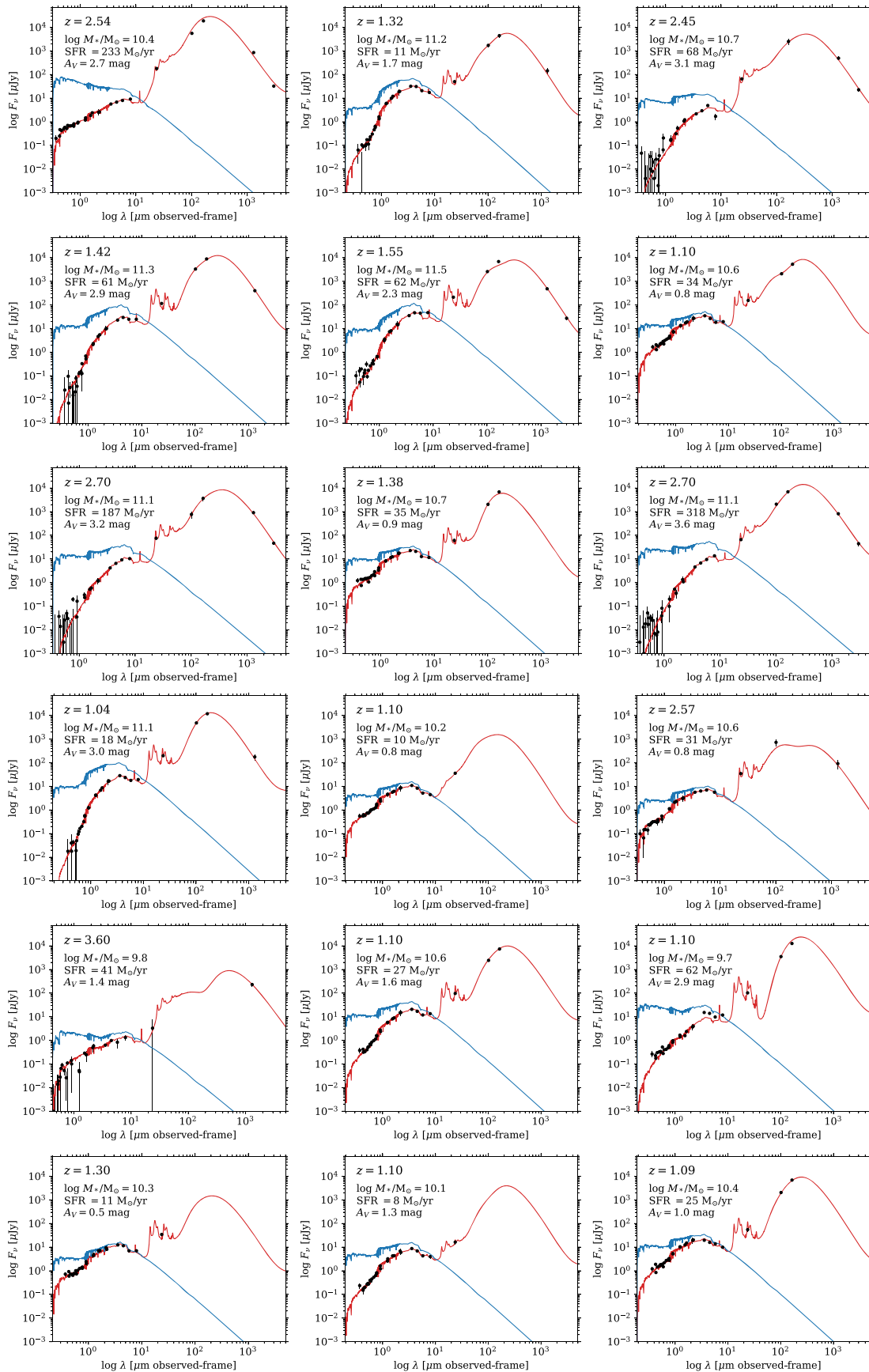


Figure 19. Spectral energy distributions (SEDs) for all the ASPECS-LP CO-detected sources from the line search (first 16) and MUSE redshift prior-based search (last 2). The black points are the observed photometry. The overall best-fit SED from MAGPHYS is shown by the red line, while the the model of the unattenuated stellar emission is shown in blue. The redshift and median values of the posterior likelihood distribution of the stellar mass (M_*), star formation rate (SFR), and visual extinction (A_V) are indicated in each panel.

ORCID iDs

Leindert A. Boogaard  <https://orcid.org/0000-0002-3952-8588>
 Roberto Decarli  <https://orcid.org/0000-0002-2662-8803>
 Jorge González-López  <https://orcid.org/0000-0003-3926-1411>
 Paul van der Werf  <https://orcid.org/0000-0001-5434-5942>
 Fabian Walter  <https://orcid.org/0000-0003-4793-7880>
 Rychard Bouwens  <https://orcid.org/0000-0002-4989-2471>
 Manuel Aravena  <https://orcid.org/0000-0002-6290-3198>
 Chris Carilli  <https://orcid.org/0000-0001-6647-3861>
 Franz Erik Bauer  <https://orcid.org/0000-0002-8686-8737>
 Jarle Brinchmann  <https://orcid.org/0000-0003-4359-8797>
 Thierry Contini  <https://orcid.org/0000-0003-0275-938X>
 Elisabete da Cunha  <https://orcid.org/0000-0001-9759-4797>
 Emanuele Daddi  <https://orcid.org/0000-0002-3331-9590>
 Tanio Díaz-Santos  <https://orcid.org/0000-0003-0699-6083>
 Jacqueline Hodge  <https://orcid.org/0000-0001-6586-8845>
 Rob Ivison  <https://orcid.org/0000-0001-5118-1313>
 Michael Maseda  <https://orcid.org/0000-0003-0695-4414>
 Jorryt Matthee  <https://orcid.org/0000-0003-2871-127X>
 Pascal Oesch  <https://orcid.org/0000-0001-5851-6649>
 Gergő Popping  <https://orcid.org/0000-0003-1151-4659>
 Dominik Riechers  <https://orcid.org/0000-0001-9585-1462>
 Joop Schaye  <https://orcid.org/0000-0002-0668-5560>
 Ian Smail  <https://orcid.org/0000-0003-3037-257X>
 Axel Weiss  <https://orcid.org/0000-0003-4678-3939>
 Paulo C. Cortes  <https://orcid.org/0000-0002-3583-780X>
 Hans-Walter Rix  <https://orcid.org/0000-0003-4996-9069>

References

- Akhlaghi, M., & Ichikawa, T. 2015, *ApJS*, **220**, 1
 Ali, B., Blum, R. D., Bumgardner, T. E., et al. 1991, *PASP*, **103**, 1182
 Aravena, M., Decarli, R., Walter, F., et al. 2019, *ApJ*, **882**, 136
 Aravena, M., Spilker, J. S., Bethermin, M., et al. 2016, *MNRAS*, **457**, 4406
 Bacon, R., Accardo, M., Adjali, L., et al. 2010, *Proc. SPIE*, **7735**, 773508
 Bacon, R., Conseil, S., Mary, D., et al. 2017, *A&A*, **608**, A1
 Bolatto, A. D., Wolfire, M., & Leroy, A. K. 2013, *ARA&A*, **51**, 207
 Boogaard, L. A., Brinchmann, J., Bouché, N., et al. 2018, *A&A*, **619**, A27
 Brinchmann, J., Charlot, S., White, S. D. M., et al. 2004, *MNRAS*, **351**, 1151
 Brinchmann, J., Kunth, D., & Durret, F. 2008, *A&A*, **485**, 657
 Caffau, E., Ludwig, H. G., Steffen, M., Freytag, B., & Bonifacio, P. 2011, *SoPh*, **268**, 255
 Carilli, C. L., & Walter, F. 2013, *ARA&A*, **51**, 1
 Chabrier, G. 2003, *PASP*, **115**, 763
 Chary, R., & Elbaz, D. 2001, *ApJ*, **556**, 562
 Conroy, C. 2013, *ARA&A*, **51**, 393
 Da Cunha, E., Charlot, S., & Elbaz, D. 2008, *MNRAS*, **388**, 1595
 Da Cunha, E., Walter, F., Smail, I. R., et al. 2015, *ApJ*, **806**, 110
 Daddi, E., Bournaud, F., Walter, F., et al. 2010, *ApJ*, **713**, 686
 Daddi, E., Dannerbauer, H., Liu, D., et al. 2015, *A&A*, **577**, A46
 Dale, D. A., & Helou, G. 2002, *ApJ*, **576**, 159
 Davies, L. J. M., Driver, S. P., Robotham, A. S. G., et al. 2016, *MNRAS*, **461**, 485
 Decarli, R., Walter, F., Aravena, M., et al. 2016, *ApJ*, **833**, 70
 Decarli, R., Walter, F., Carilli, C., et al. 2014, *ApJ*, **782**, 78
 Decarli, R., Walter, F., Carilli, C., et al. 2019, *ApJ*, **882**, 138
 Dopita, M., Fischera, J., Crowley, O., et al. 2006a, *ApJ*, **639**, 788
 Dopita, M. A., Fischera, J., Sutherland, R. S., et al. 2006b, *ApJS*, **167**, 177
 Dunlop, J. S., McLure, R. J., Biggs, A. D., et al. 2017, *MNRAS*, **466**, 861
 Eales, S., Smith, D., Bourne, N., et al. 2018, *MNRAS*, **473**, 3507
 Elbaz, D., Dickinson, M., Hwang, H. S., et al. 2011, *A&A*, **533**, A119
 Feltre, A., Bacon, R., Tresse, L., et al. 2018, *A&A*, **617**, A62
 Förster Schreiber, N. M., Genzel, R., Bouché, N., et al. 2009, *ApJ*, **706**, 1364
 Genzel, R., Tacconi, L. J., Gracia-Carpio, J., et al. 2010, *MNRAS*, **407**, 2091
 Genzel, R., Tacconi, L. J., Lutz, D., et al. 2015, *ApJ*, **800**, 20
 González-López, J., Bauer, F. E., Aravena, M., et al. 2017, *A&A*, **608**, A138
 Gonzalez-Lopez, J., Decarli, R., Walter, F., et al. 2019, *ApJ*, **882**, 139
 Haggard, D., Green, P. J., Anderson, S. F., et al. 2010, *ApJ*, **723**, 1447
 Hopkins, P. F., Richards, G. T., & Hernquist, L. 2007, *ApJ*, **654**, 731
 Hunter, J. D. 2007, *CSE*, **9**, 90
 Inami, H., Bacon, R., Brinchmann, J., et al. 2017, *A&A*, **608**, A2
 Kewley, L. J., & Dopita, M. A. 2002, *ApJS*, **142**, 35
 Kewley, L. J., & Ellison, S. L. 2008, *ApJ*, **681**, 1183
 Kewley, L. J., Geller, M. J., & Jansen, R. a. 2004, *AJ*, **127**, 2002
 Kriek, M., van Dokkum, P. G., Labbé, I., et al. 2009, *ApJ*, **700**, 221
 Leja, J., Carnall, A. C., Johnson, B. D., Conroy, C., & Speagle, J. S. 2019, *ApJ*, **877**, 140
 Leja, J., Johnson, B. D., Conroy, C., van Dokkum, P. G., & Byler, N. 2017, *ApJ*, **837**, 170
 Levesque, E. M., & Richardson, M. L. A. 2014, *ApJ*, **780**, 100
 Luo, B., Brandt, W. N., Xue, Y. Q., et al. 2017, *ApJS*, **228**, 2
 Maiolino, R., Nagao, T., Grazian, A., et al. 2008, *A&A*, **488**, 463
 Mannucci, F., Cresci, G., Maiolino, R., Marconi, a., & Gnerucci, a. 2010, *MNRAS*, **408**, 2115
 Maseda, M. V., Brinchmann, J., Franx, M., et al. 2017, *A&A*, **608**, A4
 Nagao, T., Maiolino, R., & Marconi, A. 2006, *A&A*, **459**, 85
 Noeske, K. G., Weiner, B. J., Faber, S. M., et al. 2007, *ApJL*, **660**, L43
 Oke, J. B., & Gunn, J. E. 1983, *ApJ*, **266**, 713
 Pavesi, R., Sharon, C. E., Riechers, D. A., et al. 2018, *ApJ*, **864**, 49
 Perez, F., & Granger, B. E. 2007, *CSE*, **9**, 21
 Popping, G., Decarli, R., Walter, F., et al. 2019, *ApJ*, **882**, 137
 Price-Whelan, A. M., Sipőcz, B. M., Günther, H. M., et al. 2018, *AJ*, **156**, 123
 Rafelski, M., Teplitz, H. I., Gardner, J. P., et al. 2015, *AJ*, **150**, 31
 Rakic, O., Schaye, J., Steidel, C. C., & Rudie, G. C. 2011, *MNRAS*, **414**, 3265
 Riechers, D. A., Pavesi, R., Sharon, C. E., et al. 2019, *ApJ*, **872**, 7
 Rosenberg, M. J., Van Der Werf, P. P., Aalto, S., et al. 2015, *ApJ*, **801**, 72
 Rujopakarn, W., Dunlop, J. S., Rieke, G. H., et al. 2016, *ApJ*, **833**, 12
 Saintonge, A., Catinella, B., Cortese, L., et al. 2016, *MNRAS*, **462**, 1749
 Saintonge, A., Catinella, B., Tacconi, L. J., et al. 2017, *ApJS*, **233**, 22
 Schreiber, C., Pannella, M., Elbaz, D., et al. 2015, *A&A*, **575**, A74
 Scoville, N., Aussel, H., Sheth, K., et al. 2014, *ApJ*, **783**, 84
 Scoville, N., Lee, N., Bout, P. V., et al. 2017, *ApJ*, **837**, 150
 Shapley, a. E., Steidel, C. C., Pettini, M., & Adelberger, K. L. 2003, *ApJ*, **588**, 65
 Silverman, J. D., Daddi, E., Rodighiero, G., et al. 2015, *ApJL*, **812**, L23
 Silverman, J. D., Rujopakarn, W., Daddi, E., et al. 2018, *ApJ*, **867**, 92
 Skelton, R. E., Whitaker, K. E., Momcheva, I. G., et al. 2014, *ApJS*, **214**, 24
 Sorba, R., & Sawicki, M. 2018, *MNRAS*, **476**, 1532
 Speagle, J. S., Steinhardt, C. L., Capak, P. L., & Silverman, J. D. 2014, *ApJS*, **214**, 15
 Straatman, C. M. S., Spitler, L. R., Quadri, R. F., et al. 2016, *ApJ*, **830**, 1
 Tacconi, L. J., Genzel, R., Neri, R., et al. 2010, *Natur*, **463**, 781
 Tacconi, L. J., Genzel, R., Saintonge, A., et al. 2018, *ApJ*, **853**, 179
 Tacconi, L. J., Neri, R., Genzel, R., et al. 2013, *ApJ*, **768**, 74
 Taylor, M. B. 2005, in ASP Conf. Ser. 347, *Astronomical Data Analysis and Software Systems XIV*, ed. P. Shopbell, M. Britton, & R. Ebert (San Francisco, CA: ASP), 29
 The Astropy Collaboration, Robitaille, T. P., Tollerud, E. J., et al. 2013, *A&A*, **558**, A33
 Tremonti, C. a., Heckman, T. M., Kauffmann, G., et al. 2004, *ApJ*, **613**, 898
 Van Der Walt, S., Colbert, S. C., & Varoquaux, G. 2011, *CSE*, **13**, 22
 Verhamme, A., Garel, T., Ventou, E., et al. 2018, *MNRAS*, **478**, L60
 Walter, F., Decarli, R., Aravena, M., et al. 2016, *ApJ*, **833**, 67
 Walter, F., Decarli, R., Sargent, M., et al. 2014, *ApJ*, **782**, 79
 Wang, T., Elbaz, D., Alexander, D. M., et al. 2017, *A&A*, **601**, A63
 Whitaker, K. E., Franx, M., Leja, J., et al. 2014, *ApJ*, **795**, 104
 Xue, Y. Q., Luo, B., Brandt, W. N., et al. 2011, *ApJS*, **195**, 10
 Zahid, H. J., Dima, G. I., Kudritzki, R.-P., et al. 2014, *ApJ*, **791**, 130